The Pennsylvania State University

The Graduate School

College of Earth and Mineral Sciences

OBSERVATIONS OF WAVE-TURBULENCE INTERACTIONS

IMPACTING THE STABLE BOUNDARY LAYER OVER CENTRAL

PENNSYLVANIA

A Thesis in

Meteorology

by

Astrid Suarez Mullins

Submitted in Partial Fulfillment
of the Requirements
for the Degree of

Master of Science

December 2013

The thesis of Astrid Suarez Mullins was reviewed and approved* by the following:

David R. Stauffer
Professor of Meteorology
Thesis Advisor

George Young
Professor of Meteorology and GeoEnvironmental Engineering

Nelson Seaman
Professor of Meteorology

Johannes Verlinde
Professor of Meteorology
Associate Head, Graduate Program in Meteorology

*Signatures are on file in the Graduate School

ABSTRACT

The impact of wave-turbulence interactions in the stable boundary layer is investigated using observations from a special observing network located at Rock Springs, PA. Internal gravity waves can affect the evolution and destruction of valley cold pools and produce intermittent turbulence through the modification of momentum and thermal fluxes and nonlinear phenomena (such as wave breaking or rotors). Thus, their study is crucial for improving air quality modeling and hazard predictions under stable conditions.

Six cases, characterized by nonstationarity and complex, near-surface circulations in the stable boundary layer, are identified during the spring-fall season of 2011. These cases include three synoptic regimes for which gravity waves are hypothesized. The first regime is characterized by westerly or northwesterly flow and trapped gravity waves excited by the Allegheny Mts. The second regime is characterized by a strong southerly wind component and trapped lee waves excited by Tussey Ridge. Finally, the third regime is characterized by southerly flow, weak synoptic forcing and weak near-mountain-top shear. Network measurements for the third regime suggest the presence of downslope windstorm-like motions.

Observational evidence for the existence of two types of wave-turbulence interactions, resembling that of Type 1 (associated with trapped waves) and Type 2 (associated with hydraulic-jump type events) rotor circulations, impacting the Rock Springs network are presented. It is also shown that periods of warming are typically associated with downward motion, reduced Richardson number, enhanced turbulence, positive vertical heat flux and large directional shifts (up to 180º). The largest temperature and wind speed fluctuations are associated with cases hypothesized to have the strongest nonlinear behavior. Analysis of 2-m turbulence confirms that the Richardson number is not a good measurement of stability for cases characterized by gravity wave activity. Turbulence and positive vertical heat fluxes are observed during periods when

Richardson number is much greater than 1.

In this study, observational evidence of the presence of complex wave-turbulence interactions generated by moderately complex topography (<300 m AGL) is presented. This work provides the foundation for the investigation of wave-turbulence interactions in the stable boundary layer using high resolution numerical models for real-data cases.

TABLE OF CONTENTS

LIST OF FIGURES

LIST OF TABLES

ACKNOWLEDGEMENTS

CHAPTER 1

INTRODUCTION

Under clear skies and weakly-forced synoptic conditions at night, radiative cooling contributes to the development of the stable boundary layer (SBL), a shallow, strongly stratified layer near the planetary surface. The SBL, often only tens of meters deep, is characterized by strong static stability and weak, intermittent, turbulent mixing (Mahrt 1999; Mahrt and Vickers 2002; Vickers and Mahrt 2004). Recent studies by Mahrt and Mills (2009), Mahrt et al. (2010), and Seaman et al. (2012) have shown that non-turbulent motions can be generated in the SBL by nonstationary shear events with time scales on the order of one to tens of minutes and horizontal scales ranging from the turbulent scales to the meso-gamma scales (~0.002 to 2.0 km). These motions have been described in the literature as submesoscale motions, i.e., submeso, sub-meso, or sub-mesoscale motions (e.g., Mestayer and Anquetin 1995; Finnigan 1999; Mahrt et al. 2010; Seaman et al. 2012; Mahrt et al. 2012b).

Submeso motions are of particular importance for the atmospheric transport and dispersion (AT&D) of contaminants and pollutants released in the SBL because strong stratification and very weak horizontal and vertical motions often result in persistent high concentrations of such material for several hours. However, intermittent bursts of turbulence, generated by submeso motions, can result in the enhanced dispersion of pollutants near the surface, the meandering transport of plumes, and the temporary coupling of the SBL with the residual layer—the left over mixed region above the stable layer (Zaveri et al. 1995; Salmond and McKendry 2005; Mahrt 2007). It is shown by Nappo (1991) that submeso motions are responsible for most of the exchange of heat, momentum and contaminants between the surface

and the lower atmosphere during the nighttime. Thus, the study of these motions and the mechanisms through which they modulate the SBL is crucial for improving air quality modeling and hazard predictions.

Numerous phenomena have been identified as submeso motions capable of modulating the SBL over complex topography. These include density currents, such as microfronts, katabatic flows, and solitons (e.g., Zaveri et al. 1995; Sun et al. 2002; Sun et al. 2004; Mahrt 2007; Udina et al. 2012; Mahrt et al. 2012a), and gravity waves (e.g., DeBaas and Driedonks 1985; Nappo 1991; Edwards and Mobbs 1997a and b; Brown et al. 2003; Viana et al. 2009). Much research has been conducted in order to understand the production and/or modulation of turbulence by gravity waves in the SBL, where gravity waves are often observed (e.g., Finnigan et al., 1984; Nappo and Chimonas, 1992; Nappo 2002; Grubisic and Billings 2007; Tjernstrom et al. 2009; Viana et al. 2009; Udina et al. 2012). However, there is ongoing debate regarding the dynamical effects of the waves on the evolution of turbulent fluxes in the SBL. Finnigan et al. (1984) show that, under strongly stratified conditions, intermittent turbulence generation can be explained by wave activity. Gravity waves, through nonlinear interactions, enhance the local production of turbulence (Nappo 2002; Nappo et al. 2004). In strongly stratified environments, however, turbulence is suppressed in the vertical direction by stability and destroyed by wave-modulated buoyancy effects and viscous dissipation (Steeneveld 2011). Consequently, waves can control both the production and/or destruction of turbulence through the modification of momentum and thermal fluxes and nonlinear phenomena such as wave breaking, wave-wave interactions, and rotors (Nappo 1991; Nappo 2002). These nonlinear interactions are responsible for much of the AT&D of pollutants by the waves. Therefore, the impact of gravity-wave-generated turbulence on surface measurements and the AT&D of contaminants in the SBL requires further investigation.

1.1 Internal Gravity Waves

1.1.1 Linear Theory and Its Limitations

A vast amount of research, investigating the role of gravity waves in the atmospheric boundary layer, has been conducted during the last century. However, most of what we currently know about gravity waves is based on limited observational studies and simple formulations derived from the Taylor-Goldstein equation, i.e., linear theory (Nappo 2002). The Taylor-Goldstein equation is given by

$$\frac{d^2\widehat{w}}{dz^2} + \left[\frac{N^2}{(c-u_0)^2} + \frac{u_0^{''}}{(c-u_0)} - \frac{u_0'}{H_s(c-u_0)} - \frac{1}{4H_s^2} - k^2\right]\widehat{w} = 0 \tag{1.1}$$

where $\widehat{w}$ is the wave form or Fourier transform of the vertical velocity field, N is the Brunt-Vaisala frequency, c is the phase speed of the wave along the mean flow, u_o is the mean wind speed along the direction of wave propagation, H_s is the scale height, k is the horizontal wave number, and ' and '' denote the first and second derivatives with respect to z. The first term within the brackets is known as the buoyancy term, the second term is the curvature term and the third term is the shear term (Nappo 2002). The fourth term is very small and it is commonly ignored. By also ignoring the shear term, this equation can be used to define the vertical wave number, m, given by

$$m^2 = \frac{N^2}{(c-u_o)^2} + \frac{u_o^{''}}{(c-u_o)} - k^2 \tag{1.2}$$

where the first two terms are the square of the Scorer parameter (l^2). The vertical propagation of gravity waves can be described using m. In regions where m is complex, wave motions decay with height and the waves are referred to as evanescent. In regions where m is real due to vertical

discontinuities in N or wind speed maxima, resonant trapped wave motions are permissible when the height of this ducting region is a multiple of m. The development of ducting regions is very common in the atmosphere due to the presence of low-level jets in the background flow or vertical directional shear (Nappo 2002).

Another factor that impacts the vertical propagation of waves is the presence of critical levels. Critical levels are regions where the directional component of the wind in the plane of the gravity waves vanishes (i.e., $c=u_o$) or where large directional shear is present (Nappo and Chimonas 1992). For terrain-induced gravity waves, critical levels are present when the wind component along the direction of wave propagations vanishes (i.e., $u_o=0$). Linear theory predicts wave absorption at a critical level when the Richardson number (Ri) in this region is greater than a critical value of 0.25. On the other hand, if the local Ri is less than the critical value, wave breaking and turbulence generation is predicted, and partial or total reflection can occur. Thus, deposition of wave-generated horizontal momentum is likely within this region. It is important to note that transient wave modes are only slightly modified by critical levels. These transient motions experience partial absorption of wave energy and changes in wavenumbers (Nappo 2002). Nonlinear interactions between the wave field and the mean flow at this level limit wave absorption and enhance reflection (Clark and Peltier 1977).

Linear theory has been proven successful for the theoretical study of monochromatic waves and Kelvin-Helmholtz instabilities, until the onset of turbulence, and for first order approximations of real flows. Nevertheless, the Taylor-Goldstein equation ignores the time dependence of the mean flow and nonlinear, higher order terms such as turbulent transport and products of the wave perturbation terms. These higher order terms are responsible for 1) the two-way interactions of the gravity waves and the turbulence, 2) the wave-wave interactions regulating wave harmonics, and 3) the scalar transport by wave motions relevant for AT&D. Thus by failing to account for wave-turbulence and wave-wave interactions, the attenuation of

wave stresses, and the non-steady state of the real atmosphere (Dornbrack and Nappo 1997; Nappo 2002), linear theory may be unreliable for hazard predictions in the SBL when nonlinear events are prevalent.

1.1.2   Nonlinear Wave-turbulence Interactions

Nonlinear wave-turbulence interactions have also been the subject of many observational and modeling studies. Wave-turbulence interactions have been shown to be modulated by the oscillatory part of the Reynolds stress ($\tilde{r}_{ij}$) due to the presence of wave motions. The significance of this term can be illustrated following Reynolds and Hussain (1972) triple decomposition for the wind vector, u. The triple decomposition separates the vector into a mean component, $\overline{u}$, a wave component, $\tilde{u}$, and a turbulent component, u'. Thus, the total vector would be given by

$$u_i(x_i, t) = \overline{u}_i(x_i) + \tilde{u}_i(x_i, t) + u'_i(x_i, t). \tag{1.3}$$

The mean component is obtained using time averaging, while the wave component is obtained applying phase averaging ($\langle\ \ \rangle$) for a given wave period. The remainder is considered the turbulent component. The triple decomposition and Reynold's averaging can be applied to the equations for the evolution of u in which viscous dissipation and Coriolis force are ignored and conservation of mass is assumed. These equations can be used to derive the wave and turbulent kinetic energy equations respectively, given by

$$\frac{\overline{D}}{Dt}\left(\frac{1}{2}\overline{\tilde{u}_\iota\tilde{u}_\iota}\right) = -\frac{\partial}{\partial x_j}\left[\overline{\tilde{u}_j\left(\tilde{p} + \frac{1}{2}\tilde{u}_\iota\tilde{u}_\iota\right)}\right] + \left(-\overline{\tilde{u}_\iota\tilde{u}_j}\frac{\partial U_i}{\partial x_j}\right) + \overline{\tilde{r}_{\iota j}\frac{\partial\tilde{u}_\iota}{\partial x_j}} - \frac{\partial}{\partial x_j}\left(\overline{\tilde{u}_\iota\tilde{r}_{\iota j}}\right)$$
$$+ \frac{g}{\Theta}\overline{\tilde{\theta}\tilde{u}_\iota}\delta_{i3} \tag{1.4}$$

and

$$\frac{\overline{D}}{Dt}\left(\frac{1}{2}\overline{u_\iota'u_\iota'}\right) = -\frac{\partial}{\partial x_j}\left[\overline{u_j'\left(p' + \frac{1}{2}u_\iota'u_\iota'\right)}\right] + \left(-\overline{u_\iota'u_j'}\frac{\partial U_i}{\partial x_j}\right) - \overline{\tilde{r}_{\iota J}\frac{\partial\tilde{u}_\iota}{\partial x_J}} - \frac{\partial}{\partial x_j}\left(\frac{1}{2}\overline{\tilde{u}_\iota\tilde{r}_{\iota J}}\right)$$

$$+\frac{g}{\Theta}\overline{\theta'u_\iota'}\delta_{i3}$$

(1.5)

where

$$\frac{\overline{D}}{Dt} \equiv \frac{\partial}{\partial t} + \bar{u}_j\frac{\partial}{\partial x_j},$$

(1.6)

$$\tilde{r}_{ij} \equiv \langle u_i'u_j'\rangle - \overline{u_i'u_j'},$$

(1.7)

p is the pressure, g is the gravitational force, and θ and Θ are the perturbation and mean potential temperature respectively. The $\overline{\tilde{r}_{\iota J}\frac{\partial\tilde{u}_\iota}{\partial x_J}}$ term represents the rate of work of wave-modified Reynold stress against the wave rate of strain. Thus, this term is responsible for the energy transfer between the turbulence and the wave and vice-versa.

Papers by Einaudi and Finnigan (1981), Finningan et al. (1984), and Fua et al. (1982) identify three wave-turbulence coupling regimes: 1) one regime with limited energy transfer between the mesoscale flow and turbulent scales, in which wave motions appear to modulate the surface turbulent fluxes; 2) a second regime in which wave-turbulence interactions dominate energy transport from the high amplitude wave modes to the turbulence; and 3) a final regime in which turbulence acts to extract energy from the mean flow, further amplifying the gravity wave. Overall, numerous mechanisms through which gravity waves can interact significantly with or generate turbulence have been identified through theoretical and modeling work. These include 1) critical level interactions, 2) wave breaking, 3) convective instabilities, and 4) rotor circulations (Einaudi and Finnigan 1981; Doyle and Durran 2007). These processes are not

mutually exclusive; therefore, complex interactions among them and other wave processes such as rolls, wave packets, and wave harmonics can be present at a particular time.

One of the most studied wave-turbulence mechanisms is the generation of turbulence due to wave activity at critical levels. Waves approaching a critical level experience increased shear; this locally reduces the *Ri* below critical levels, indicating the production of turbulence (Nappo 2002). Theoretical and modeling work by Booker and Bretherton (1967), Fritts (1978), Finnigan and Einaudi (1981), and Nappo and Chimonas (1992) suggest that wave amplification near critical levels can result in shear instabilities and enhanced turbulent fluxes near the surface. Fritts (1978) shows that these nonlinear, wave-critical-level interactions stabilize the flow above the critical level, but destabilize the mean flow below. These modifications of the background flow result in the downwards shift of shear instabilities and turbulence. Numerical model studies by Clark and Peltier (1977, 1984) suggest that low-level, wave resonance and amplification are possible when the height of the critical level equals ¾λ, where λ is the horizontal wavelength, due to the superposition of wave disturbances. This mechanism aids the amplification of the low-level waves and enhances the production of turbulence at low levels. In addition, the amplification of waves due to critical level resonance has been linked to the development of downslope wind storms, such as those observed over Boulder, Colorado (e.g., Clark and Peltier 1984). Consequently through various mechanisms, wave-critical-level interactions can enhance the production of turbulence within the SBL. The development of these turbulent layers can produce intermittent turbulent outbursts when coupled with the surface. Observations by Tjernstrom et al. (2009) have verified the existence of enhanced–turbulence regions in the nocturnal SBL and residual layers due to the presence of one or more critical levels.

A more direct interaction between gravity waves and turbulence is through wave breaking. Wave breaking occurs when wave growth becomes unbounded at some critical height, leading to the overturning of the isentropes and the development of local instabilities that break

a)

b)
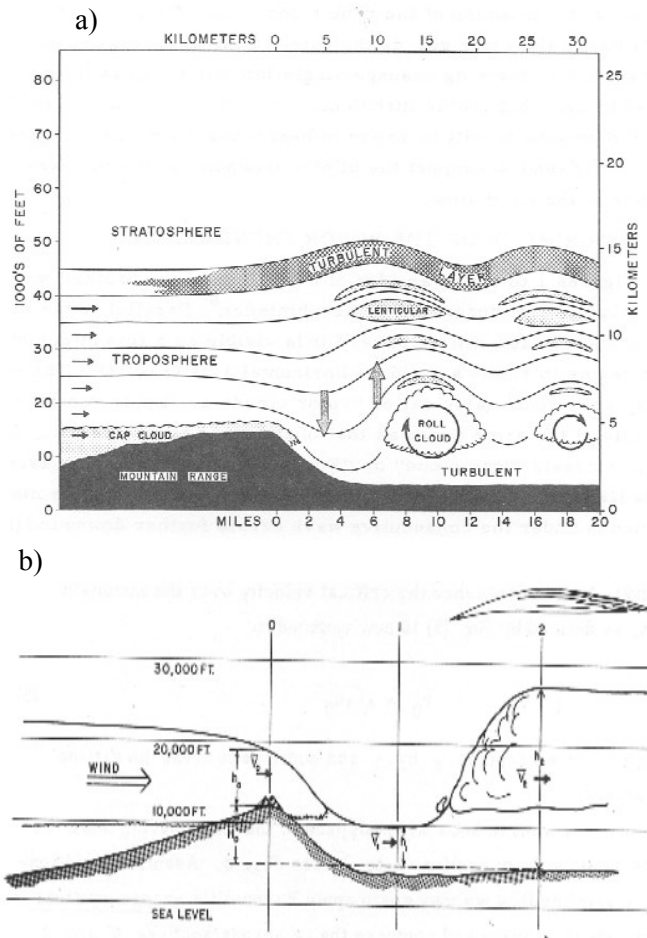
Figure 1-1. Schematic diagrams of Type 1 (a) and Type 2 (b) rotors, retrieved from Kuettner (1959).

down into small-scale turbulence. This problem is fairly well understood, and two primary mechanisms have been identified: shear instabilities, such as Kelvin-Helmholtz waves, and Jeffrey's roll-wave instabilities (Jeffrey 1925). Shear instabilities are characterized by two-layer flow with different speeds, where small-scale perturbations result in the generation, amplification, and subsequent overturning of the waves (Nappo 2002). This mechanism has been well documented in the literature (e.g., Finnigan and Einaudi 1981; Finnigan et al. 1984; Blumen et al. 2001; and Newson and Banta 2003). A less studied mechanism is Jeffrey's roll-wave instabilities in the atmospheric boundary layer. This type of instability, resulting from the balance between wave-induced pressure gradients and surface drag, supports lasting states of overturning

(Chimonas 1993). Chimonas (1993, 1994) suggest wave amplification, due to Jeffreys' instabilities, is responsible for the transfer of available energy at larger scales to the dissipation scales. It is noted by Chimonas (1994) that mechanical shear is the predominant turbulence-generating mechanism. Turbulence generated by gravity wave breaking has been shown by Blumen et al. (2001) and Newson and Banta (2003) to be diffused downward resulting in temporary increases in surface turbulent fluxes.

Lastly, rotor circulations have long been known to be a source of turbulence in the SBL when gravity wave activity is present. Rotors are boundary-layer processes characterized by low-level vortices that parallel the topography (e.g., Doyle and Durran 2002; Grubisic and Billings 2007). These vortical structures are commonly present along the crests of quasi-two-dimensional waves excited by narrow, elongated ridges (Doyle and Durran 2002). The size of these disturbances can vary from hundreds of meters to a few kilometers. Over the last several decades theoretical, observational, and modeling studies have identified some of the dynamical mechanisms leading to rotor development. Early works by Kuettner (1959) and Lester and Fingerhut (1974), among others, have allowed the identification of two types of rotor circulations: 1) Type 1, characterized by moderate or severe turbulence, where the rotor circulation becomes collocated beneath the resonant wave crest (Fig 1-1a); and 2) Type 2, characterized by severe to extreme turbulence associated with high-amplitude waves, resembling hydraulic jumps and/or downslope wind storms (Fig 1-1b), such as those described by Smith (1979 and 1989).

Rotors have been shown to be a boundary-layer separation process, enhanced by wave-driven pressure gradient fluctuations and surface drag (Doyle and Durran 2002). Doyle and Durran (2002) show a strong correlation between the pressure perturbations induced by the waves and the intensity of rotor circulation. Two- and three-dimensional simulations have shown surface friction to generate a layer of horizontal vorticity that is lifted by the waves at the boundary layer separation point (Doyle and Durran 2002; Doyle and Durran 2007). Rotors then

generate turbulence through shear and convective instabilities. Studies by Vosper (2004) and Hertenstein and Kuettner (2005) look at the effect of the wind profile and topography on rotor circulations using a two-dimensional model. These studies illustrate the role of the shear profile in the upstream inversion for the development of Type 1 or Type 2 rotors. It is shown by Hertenstein and Kuettner (2005) that a strong sheared profile within a near-mountain top inversion leads to the development of Type 1 rotors while a weaker shear profile within a near-mountain-top inversion leads to Type 2 rotors. Hertenstein (2009) addresses the role of the near-mountain-top inversion in the development of both rotor types. Moderate inversions are shown to be conducive to Type 1 rotors while strong near-mountain-top inversions are associated with Type 2 rotor circulations.

Rotor circulations have been addressed only by a handful of studies compared to the large volume of research dealing with gravity waves. These include observational field campaigns (e.g., the Sierra Rotor Project (SRP) over the Sierra Nevada Mts. during the spring of 2004 (Grubisic and Billings 2007), the field campaign over Wickham Mountain on the Falkland Island (Mobbs et al. 2005), and the Terrain-induced Rotor Experiment (T-REX) over the Sierra Nevada during the spring of 2006. Numerical studies have been conducted for idealized cases (e.g., Doyle and Durran 2002; Vosper 2004; Hertenstein and Kuettner 2005; and Smith and Skyllingstan 2009) and observed events (e.g., Sheridan and Vosper 2006, Grubisic and Billings 2007, Gohm et al. 2008, Doyle et al. 2009). Nevertheless, further research is needed in order to investigate the impact of three-dimensional topography, inversion depth and strength, and flow regime on real case studies.

All of the aforementioned mechanisms have been hypothesized to produce wave-modulated turbulence, resembling an upside-down boundary layer above the surface, as described by Mahrt and Vickers (2002). The temporary coupling of elevated turbulence with the surface can also be responsible for the intermittent turbulence often observed in the SBL. However,

a)   b)
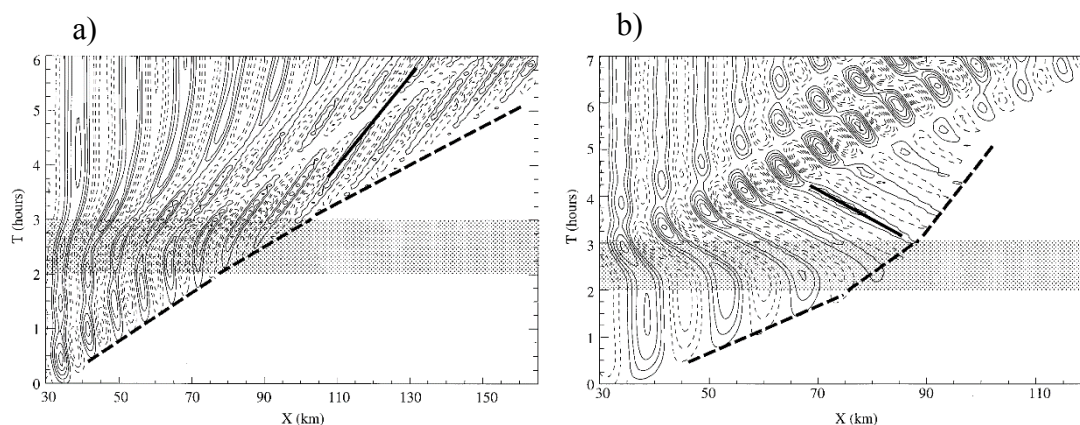
Figure 1-2. Hovmoller diagrams of vertical velocity illustrating wavelength transitions a) from a strongly stable to weakly stable and b) from weakly stable to strongly stable, after Nance and Durran (1997).

despite the significant implications of these motions for AT&D, their study in the nighttime stable regimes has been limited or ignored.

1.1.3 Nonstationarity of Gravity Waves

The nonstationarity of gravity waves (i.e., temporal variations of wave properties) in the atmospheric boundary layer have been the focus of many studies, including Ralph et al. (1997) and Nance and Durran (1997, 1998) to name a few. Observational analyses have revealed the existence of three basic types of nonstationarity: 1) downstream drifting of the wave pattern, 2) changes in horizontal wavelength, and 3) changes in the location and amplitude of local ridges and troughs (Nance and Durran 1997). An observational study by Ralph et al. (1997) focusing on transient, boundary-layer-trapped waves in the daytime planetary boundary layer (PBL) shows rapid variations of up to 30 % h^{-1} in the horizontal wavelength. A survey of 24 nonstationary wave events conducted by Ralph et al. (1997) reveal similar lengthening of wavelength over the Sierra Nevada Mts. (e.g., Collis et al. 1968), the Colorado Rocky Mts. (e.g., Vergeiner and Lilly 1970), and the Appalachian Mts. (e.g., Weiss 1976). Four of the 24 cases surveyed show wavelength decreasing up to 43 % h^{-1} through the late afternoon and early evening. Nevertheless,
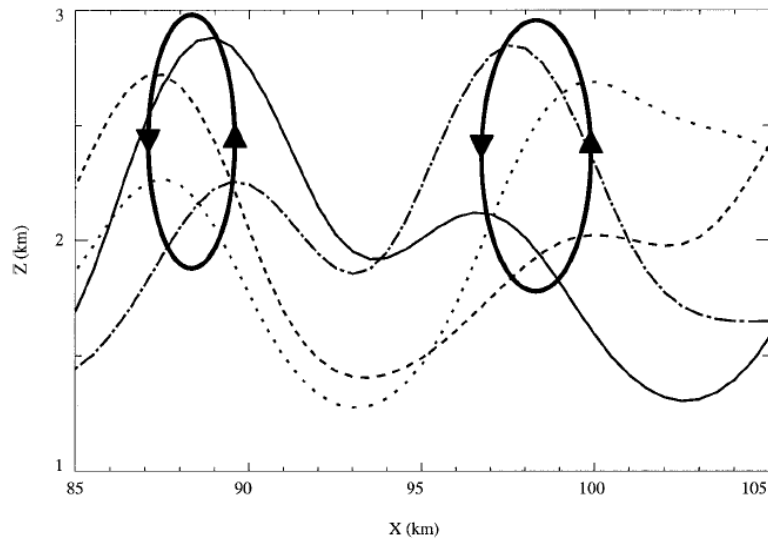
Figure 1-3. Potential temperature isentropes plotted every 20 min (solid, long-dash, short-dashed, dash-dotted curves) for case exhibiting steady state background conditions and nonlinear wave motions. Retrieved from Nance and Durran (1998).

Ralph et al. (1997) show that both kinds of transitions, lengthening and shortening of wavelength, are highly dependent on the time evolution of the background flow.

The effects of wavelength lengthening and shortening of wave harmonics are illustrated by Nance and Durran (1997, 1998) using numerical simulations of nonstationary, two-dimensional, background conditions. Nance and Durran (1997) examine two wavelength transitions: 1) 1-h transition from a strongly stratified to a weakly stratified ducting region (Figure 1-2a), and 2) 1-h transition from a weakly stratified to a strongly stratified ducting region (Figure 1-2b). During the transition from strongly stratified to weakly stratified, the original resonant wave pattern detaches from the topography and propagates downstream retaining its original structure. However, the resonant waves excited after transition create a divergent wave packet that overtakes the original resonant waves. This transition is shown to be well predicted by linear theory. During the transition from weakly stratified to strongly stratified, the phase velocity of the waves before the transition is greater than that after transition. In this case, the new resonant waves overtake the initial wave pattern through the superposition of waves. Nance and Durran

(1997) show wavelength shortening to result in wave amplification, due to constructive interference and stronger vertical motions. This study suggests that changes in static stability alone are not sufficient to produce wavelength transitions over short time scales. However, the authors note that other mechanisms such as changes in background wind, cross mountain gradients or non-uniform forcing can produce the model-predicted, rapid wavelength transitions.

The nonstationarity of lee waves is often associated with changes in the background flow. Nevertheless, Nance and Durran (1998) show that nonlinear, trapped, gravity waves exhibit temporal variations in wavelength and amplitude despite steady-state background fields. Nonlinear effects excite elliptical oscillations of the crests and troughs, typically 180º out of phase with adjacent cycles as depicted in Figure 1-3. It is shown that nonlinear wave dynamics can generate a multiplicity of trapped modes that can interact to produce more realistic fluctuations. Using simple models, Nance and Durran note that the small and irregular variations of wavelength and amplitude often observed in trapped lee waves are more likely generated by nonlinear wave-turbulence interactions than changes in the background flow.

Thus, the observed nonstationarity of gravity waves in the atmosphere can be the result of changing background flow conditions or the presence of nonlinear interactions. Constructive interference due to wavelength transition can act to amplify the wave and lead to wave breaking. The generation of turbulence due to breaking wave modes can impact both the development and evolution of the SBL and underlying cold pools.

1.2 Observational Limitations in the Study of Gravity Waves in the SBL

Despite our current understanding of nonlinear wave interactions, the study of these processes in the SBL presents numerous observational challenges. The study of gravity waves in the SBL is complicated by the questionable utility of stability parameters, such as the Ri, in stable

regimes and weak wind conditions. In the SBL, turbulence has been shown to persist as the local *Ri* increases well above the critical value of 0.25, estimated from linear instability analysis (Einaudi and Finnigan 1993; Mahrt et al. 2012b; Sun et al. 2012). The *Ri* does not account for the many nonlinear and unsteady motions often present in the SBL. Thus, a critical *Ri*, derived from linear analysis, is not a representative parameter for the onset of turbulence when nonlinear interactions are present.

The study of wave-turbulence interactions in the SBL is further complicated by the fact that wave and turbulent signals are neither local nor confined to the stable layer since pressure measurements reflect changes in the entire column rather than just at the observation level. Thus, surface time series collected by an *in-situ* tower measurement can also detect wave activity at the upper levels as well as within the SBL. Furthermore, gravity waves in the atmosphere often do not exhibit well-defined periodicity. These "dirty waves" typically exhibit a wide range of frequencies and amplitudes, varying in time and space, perhaps extending for only one wavelength and thus making wave signal processing very challenging.   In the case of mountain-lee waves, for example, the observation is further complicated by the fact that waves are quasi-stationary and locked to the terrain.   Tower and surface measurement units are typically stationary; thus they cannot measure large fluctuations in the pressure or wind fields since they always sample the same region of the wave train for these quasi-stationary waves.   Thus, common signal-processing approaches are not adequate for their study.

Finally, field campaigns studying the SBL and nonlinear wave-turbulent interactions tend to be 'unrepresentative' or site specific (Salmond and McKendry 2005). As noted by Mahrt et al. (2012a), the generation of turbulent modes and their interaction with the strongly stratified layer are largely driven by site characteristics such as topography. Similar topographical dependencies are found by Grubisic and Billings (2007) for the development of nonlinear wave behavior. Consequently, the results of previous studies and formulations are difficult to generalize for the

SBL. These observational limitations have hampered both the study of wave-turbulence interactions and the development of better parameterizations for the SBL.

1.3 Thesis Objectives

This thesis is the first part of a combined observational and modeling study investigating the effect of trapped, nonlinear, gravity waves on near-surface measurements over the moderately complex terrain of Central PA. In this first part, the impact of wave-turbulence interactions on the generation of intermittent turbulent bursts and the modulation of the surface cold pool is investigated using observations from a special network located at Rock Springs, PA. Favorable synoptic conditions for the development of gravity wave motions that can impact the observing network are identified using North American Regional Reanalysis (NARR), standard rawinsonde soundings, surface observations at University Park Airport, PA, and the Rock Springs, PA observations. Six cases, covering three synoptic regimes, are identified and investigated.

This thesis is organized as follows. Chapter 2 summarizes the instrumentation, network design, case selection and experimental design. Chapter 3 includes a description of synoptic and mesoscale conditions and network observations, and analysis of wave-turbulence interactions for the case studies. Finally, a summary, concluding remarks, and future work are provided in Chapter 4.

CHAPTER 2

OBSERVATIONS, CASE SELECTION, AND EXPERIMENTAL DESIGN

The impact of wave-turbulence interactions on the SBL is examined in case-study mode observational analyses. Section 2.1 provides a comprehensive description of the observing network, instrumentation, and data. In Section 2.2, case selection, the experimental design and data analysis strategies are presented.

2.1 Rock Springs, , Observation Network

An observing network is deployed at Rock Springs, Pennsylvania, in order to investigate the source and evolution of wave-wave and wave-turbulence interactions in the SBL over the moderately complex terrain of Central PA. In this region, gravity waves are common under stable conditions, since their development is aided by the local, complex topography. Central PA is characterized by narrow, quasi-parallel, southwest-to-northeast-oriented ridges that stand between 200 and 700 m above the adjacent valley floors. The Rock Springs network is located within the Nittany Valley in Central PA, approximately 20 km southeast of the Allegheny Mountains (~500 m above the valley floor and 15-20 km in width) and adjacent to Tussey Ridge (~300 m above the valley floor and 3 km width) (Fig. 2-1). This region is primarily characterized by croplands and grasslands on the valley floor and forested areas along the upper slopes of Tussey Ridge and other elevated terrain features. The location of the observing network permits the study of trapped lee waves, excited by both the Allegheny Mts. and Tussey Ridge, among other submeso motions. Observations from this network have been used to analyze turbulent motions in the SBL, to examine cold pool development and evolution, and to verify high-
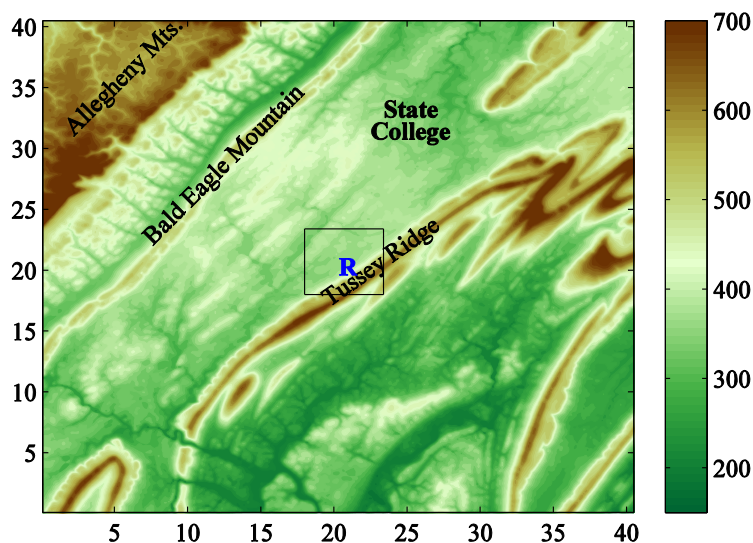
Figure 2- 1. High-resolution (90-m) terrain elevation (m MSL, shaded according to scale on right) for a 40 km by 40 km region containing the Rock Springs network in Central PA.   The network is denoted by the blue R, and major topographical features are labeled.   Black square denotes the instrumented region shown in Fig. 2-2.

resolution simulations of the SBL (e.g., Mahrt et al. 2010; Mahrt et al. 2012a and b; and Seaman et al. 2012).

The Rock Springs network currently consists of an array of 2-, 10-, and 50-m above ground level (AGL) towers and two sonic detection and ranging instruments (SODARs) distributed over a 3-km long region to the north of Tussey Ridge (Fig. 2-2).   Four 2-m instrumented towers (Sites 3, 6, 7, and 12), three 10-m instrumented towers (Sites 5, 8, and 9), and a 50-m tower (Site 10) are used to sample the SBL and wave activity at various heights. A summary of the tower locations and instrumentation is provided in Table 2-1.

All of the sites are equipped with Campbell Sci. T107 thermistors at the heights reported in the table. These instruments measure 1-min-averaged temperature from 1 Hz sample data with accuracy better than ±0.4ºC (Campbell Sci 2012). Additional temperature measurements are also available within the network at Site 9. This site is equipped with Omega Engineering TMTSS-020G thermocouples at 1, 1.5, 2, 3, 4, 5, 6, 8, and 10 m AGL. Temperature is sampled by these instruments with a 1 Hz frequency and ±1ºC standard limits of error (Omega Engineering 2013).
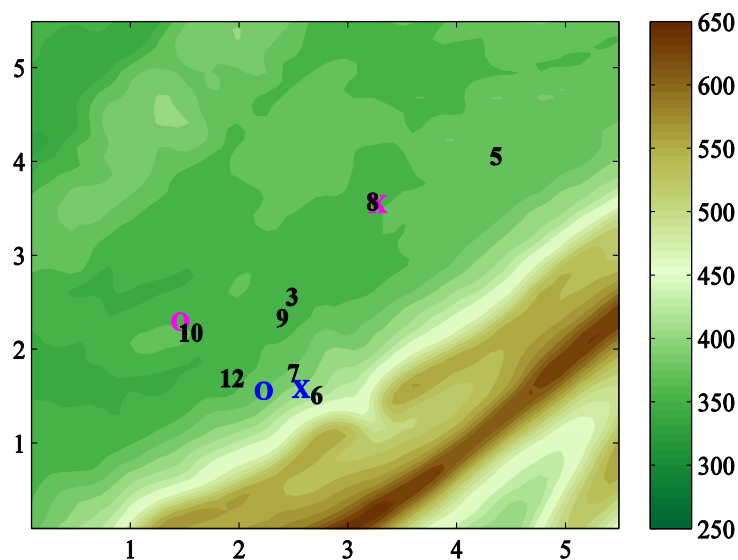
Figure 2- 2. Distribution of instrumented towers and SODARs within a 5 km by 5 km region containing the Rock Springs network. X and O represent the locations of SODAR 2028 and 2027 respectively before (blue) and after (magenta) 29 September 2011, respectively.

Wind measurements within the network are obtained from Vaisala WS425 2-D sonic anemometers and high-frequency (20 Hz) Campbell Sci. CAST3 3-D sonic anemometers. The 2-D sonic anemometers measure 1-min averaged horizontal wind components, from which wind speed and direction are derived. These instruments record wind speed measurements with an accuracy of ± 0.1 ms^{-1} and wind direction with an accuracy of $\pm 2°$ (Vaisala 2010). The 3-D sonic anemometers sample u, v and w. The horizontal and vertical wind-component measurement precision of the instruments is ± 0.001 ms^{-1} and ± 0.005 ms^{-1} respectively (Campbell Scientific 2013).   The use of these fast response instruments is needed in order to compute the turbulence and record the sudden wind shifts often observed in the SBL under light wind conditions.

In addition to the array of towers, two WindExplorer 4500 Hz SODARs, manufactured by Atmospheric Science Corporation, are deployed within the network. These instruments measure u, v, w, and wind-component variances, with wind speed accuracy of ± 0.5 ms^{-1} and wind direction accuracy of $\pm 2°$ for wind speeds greater than 2 m s^{-1}(Atmospheric Systems Corporation 2013). The SODARs can detect 3-D motions at ranges from 30 m up to ~250 m AGL with a

Table 2-1. Instrumentation information for the Rock Springs Network.

Sites	Lat N	Lon W	Elev. (m)	Instrumentation	Data Res.	Height(m)
3	40.71035	77.95762	368	Thermistor	1 min	2
				2-D sonic	1 min	2
5	40.72029	77.93098	378	Thermistor	1 min	2
				2-D sonic	1 min	9
6	40.70042	77.95728	416	Thermistor	1 min	2
				2-D sonic	1 min	2
7	40.70296	77.95925	385	Thermistor	1 min	2
				2-D sonic	1 min	2
				3-D sonic	0.05 s	2
8	40.71816	77.94582	364	Thermistor	1 min	2,9
				2-D sonic*	1 min	9
				3-D sonic	0.05 s	2
9	40.70848	77.95892	368	Thermistor	1 min	2, 5, 9
				2-D sonic*	1 min	2
				3-D sonic	0.05 s	1,2,8.5
				Thermocouple**	0.05 s	0.5,1,1.5,2, 3, 4, 5, 6, 8, 10
10	40.70885	77.97009	367	Thermistor	1 min	17
				2-D sonic	1 min	17
				3-D sonic	0.05 s	33, 47
12	40.70369	77.96681	363	Thermistor	1 min	2
				2-D sonic	1 min	2

* Data available until 22 August 2011
**Thermocouple data available after 22 August 2011

vertical resolution of 5 m. For this thesis, SODAR winds and variances are averaged over a 10-min period. SODAR-derived winds and variances can be useful for both sampling the SBL and establishing correlations between elevated disturbances and low level motions detected by the tower measurements. Prior to 29 September 2011, the SODARs were located on the slope of Tussey Ridge, approximately 177 m and 370 m south and west-southwest of Site 7, respectively. After this date, SODARs 2027 and 2028 are located near Site 8 and Site 10 to sample motions above the valley floor (Fig 2-2).

2.2 Case Selection and Experimental Design

Rock Springs network observations, University Park Airport (KUNV) measurements, soundings and NCEP North American Regional Reanalysis (NARR; Mitchell et al. 2004) are used to identify six cases characterized by clear skies, weak-wind conditions and terrain-induced gravity waves over the observing network. NARR data are 32-km, grid-spaced reanalyses produced from NCEP Eta model output and observations, including land surface data, satellite fields, and orographically-corrected precipitation, originally developed in order to provide better estimates of hydrologic variables (Luo et al. 2005). NARR data and nearby soundings are used to define the "large scale" conditions while thermistor, 2-D and 3-D sonic anemometers, and SODAR data are used to link near-surface temperature and wind fluctuations to nonlinear wave interactions, such as wave breaking, wavelength transitions, and rotor circulations.

Six cases spanning three types of terrain-induced gravity wave phenomena impacting the Rock Springs network are identified during the 2011 spring, summer and fall seasons. The wave type and wave disturbance source for each case study are summarized in Table 2-2. These include; 1) trapped-lee waves excited by the Allegheny Mts., including 14 April 2011 (APR14) and 16 September 2011 (SEP16); 2) trapped lee waves excited by Tussey Ridge, including 6 November 2011 (NOV06) and 04 December 2011 (DEC04); and 3) highly nonlinear gravity waves, resembling hydraulic jumps and/or downslope windstorms, excited by Tussey Ridge,

Table 2-2 Summary of Cases

Wave Type	Source of Disturbance	Cases
Resonant Lee Waves/Type I	Allegheny Mts.	APR14
		SEP16
	Tussey Ridge	NOV06
		DEC04
Downslope Windstorm/Type II	Tussey Ridge	AUG24
		NOV13

including 24 August 2011 (AUG24) and 13 November 2011 (NOV13). All of the cases exhibit temperature and wind speed fluctuations and wind directional shifts in the SBL with time scales ranging from tens of minutes (min) to hours (h) throughout the night.

For all the case studies, wave-turbulence interactions are assessed through the examination of thermistor, 3-D sonic, and SODAR data. Wave-modulated turbulence is identified using three parameters: 2-9 m AGL bulk Richardson number (Ri_b), 2-m vertical heat flux, and 2-m *TKE*. Here, a finite-difference form of the Ri_b is used, given by

$$Ri_b = \frac{g\Delta z(\Delta\theta)}{\Theta(\Delta u^2 + \Delta u^2)} \tag{2.1}$$

where g is the acceleration due to gravity, θ is potential temperature, and u and v are the horizontal wind components The Ri_b is computed using 12-min center-averaged quantities between 2 and 9 m AGL. Similarly, 12-min-averaged vertical heat fluxes and *TKE* are computed using Reynolds averaging (e.g., $u = \bar{u} + u'$) and a time-averaging window of 1 min. These quantities are given by

$$\overline{w'\theta'} = \overline{(w - \bar{w})(\theta - \bar{\theta})} \tag{2.2}$$

and

$$TKE = \frac{1}{2}(u'^2 + v'^2 + w'^2) \tag{2.3}$$

where ‾ denotes mean quantities and ' denotes perturbations from the mean, and w is the vertical motion. It is important to note that time averaging windows of 36 s have been previously used by Mahrt et al. (2012b) for the study of turbulent motions in the SBL at Rock Springs. All of the

cases examined by Mahrt et al. (2012b) are very stable and present 6-h averaged Ri_b greater than 1. In this study, a larger range of Ri_b, extending from weakly stable to very stable, is considered; thus a longer averaging window of 1 min for the wind components is used to produce the 12-min averages of the heat flux and *TKE*. Nevertheless, flux computations exhibit little sensitivity to time averaging for windows slightly shorter or longer than 1 min (not shown).

CHAPTER 3

OBSERVATIONS AND ANALYSIS OF WAVE-TURBULENCE INTERACTIONS IN THE SBL

In this chapter, NCEP reanalyses and Rock Spring network observations are used to examine six gravity-wave events characterized by weak winds and varying degrees of stability. Three terrain-generated wave scenarios are examined: 1) trapped lee waves excited by the Allegheny Mts., 2) trapped lee waves excited by Tussey Ridge, and 3) highly nonlinear waves, resembling a hydraulic jump or downslope windstorm excited by Tussey Ridge. Two case studies are presented for each of the three regimes.

3.1 Resonant Lee Waves Excited by the Allegheny Mts.: APR14 and SEP16

APR14 and SEP16 are examined in order to identify nonlinear interactions in the SBL over the Rock Springs network. Synoptic and mesoscale patterns are examined for the development of trapped gravity waves excited by the Allegheny Mts. In addition, Rock Springs observations are analyzed to assess the impact of Allegheny Mts. gravity waves on the development and evolution of the local SBL.

3.1.1 Synoptic Conditions

APR14 is characterized by an upper-level long wave trough and low pressure system moving off the Northeast coast of the USA (Fig 3-1). The 500-hPa winds are predominantly northwesterly, associated with a long wave trough located over northern New York at 0000 UTC and moving northeastwards in time (Fig 3-1e and f). At this level, wind speed over Central PA

weakens from 20 m s^{-1} to 10 m s^{-1} over the 12-h night period. At 850 hPa, winds change from northwesterly at 0000 UTC to northerly by 1200 UTC, over Central PA (Fig 3-1c and d). As the surface low-pressure system, located over New Jersey at 0000 UTC moves into the western Atlantic, decreasing surface pressure gradients and wind speeds are observed over the network (Fig 3-1a and b). Surface wind directions, however, remain predominantly from the northwest through most of the night. NARR-derived cloud fraction reveals a dense-cloud covered region, associated with the surface low-pressure system, extending through most of eastern PA. Cloud cover fraction decreases over time as the low pressure system moves offshore. KUNV reports low-level cloud coverage at 500 to 800 m mean sea level (MSL) from 0000 to 0500 UTC and wind speed less than 2.6 m s^{-1} through most of the night (not shown).

The first few hours of the night are characterized by weak directional shear with height due to strong, predominantly-northwesterly winds. However, as the upper level flow weakens and the 850-hPa winds become more northerly, a region of veering winds develop, extending from the surface up to 850 hPa. The large wind directional shear with height contributes to the development of a duct within this region that traps gravity wave excited by the local topography. Low level northwesterly flow, increasing stability and directional shear through the night support the development of gravity wave within Central PA for this case. Thus, gravity wave motions, excited by the Allegheny Mts., can be expected to impact the downwind Rock Springs network through the latter period of the night.

The SEP16 case features westerly wind components through most of the night (Fig 3-2a-f). The 500-hPa flow is strongly westerly over central PA, with wind speeds ranging between 25 to 35 m s^{-1}. The 850-hPa flow is characterized by weakening pressure gradients over the Northeast as a high pressure system moves into the region and weak (< 10 m s^{-1}) north-northwesterly winds by 1200 UTC. At the surface, the flow is also north-northwesterly and is characterized by weakening pressure gradients and wind speeds as high pressures moves over the

region. The skies are mainly clear through most of the night. KUNV reports scattered clouds, at
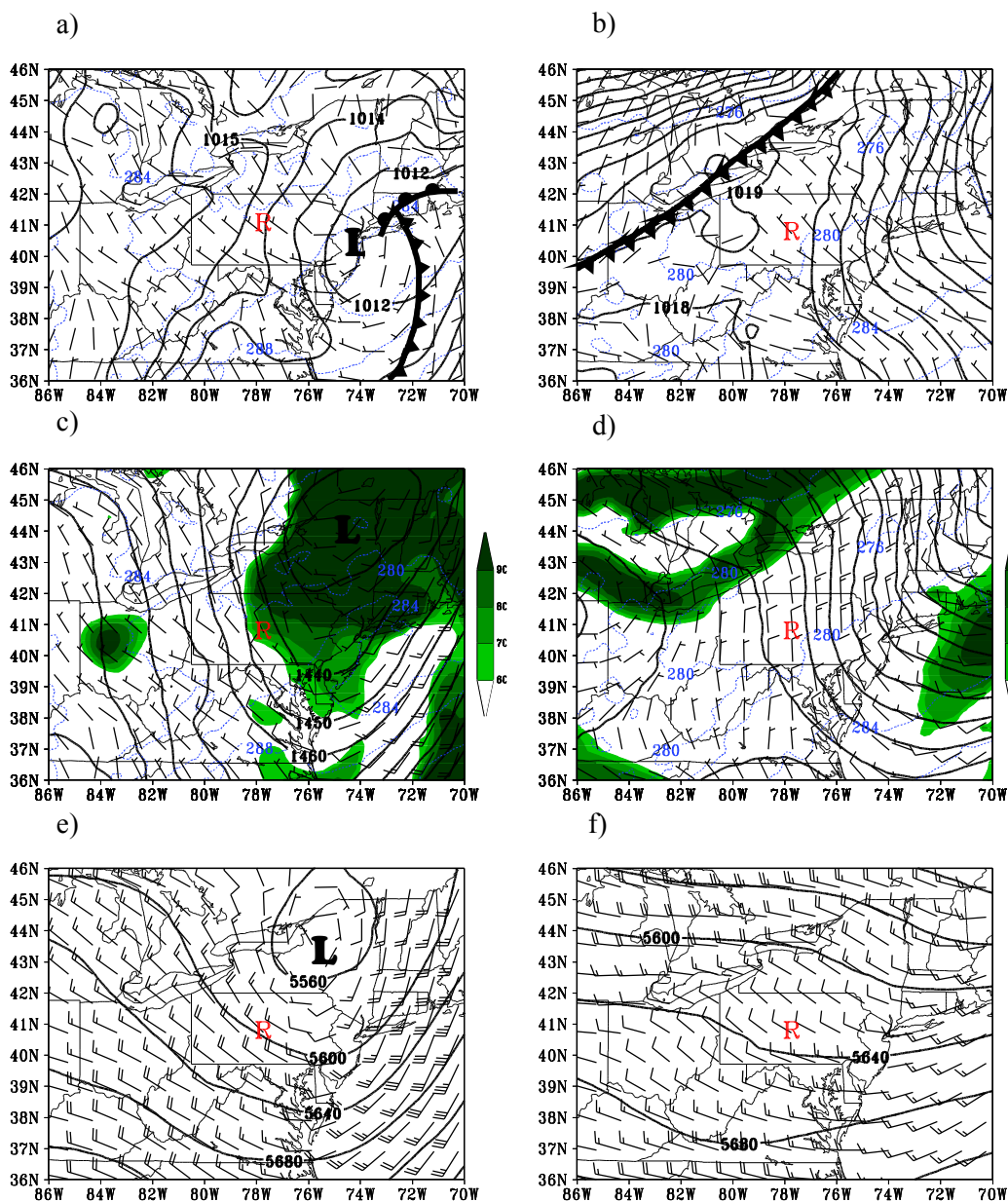
Figure 3-1. NARR reanalysis at 0000 UTC (a, c, and e) and 1200 UC (b, d, and f) for APR14 of surface pressure (black; contoured every 1hPa), temperature (blue; contoured every 4 K), and winds barbs (m s^{-1}) (a and b); 850-hPa geopotential heights (black; contoured every 10 m), temperature (blue; contoured every 4 K), total cloud fraction (shaded according to scale), and wind barbs (m s^{-1}) (c and d); and 500-hPa geopotential heights (black; contoured every 40 m) and wind barbs (m s^{-1}) (e and f). The location of the Rock Springs network is marked by a red R.

elevations ranging from 2000 to 3000 m, from 0400 to 1000 UTC.

The flow through the period is primarily north-northwesterly at the surface and 850 hPa backing to westerly at 500 hPa. The NARR data and Pittsburgh Airport (KPIT) soundings (not shown) reveal a directional shear maximum between 600 and 500 hPa at 0000 UTC that descends
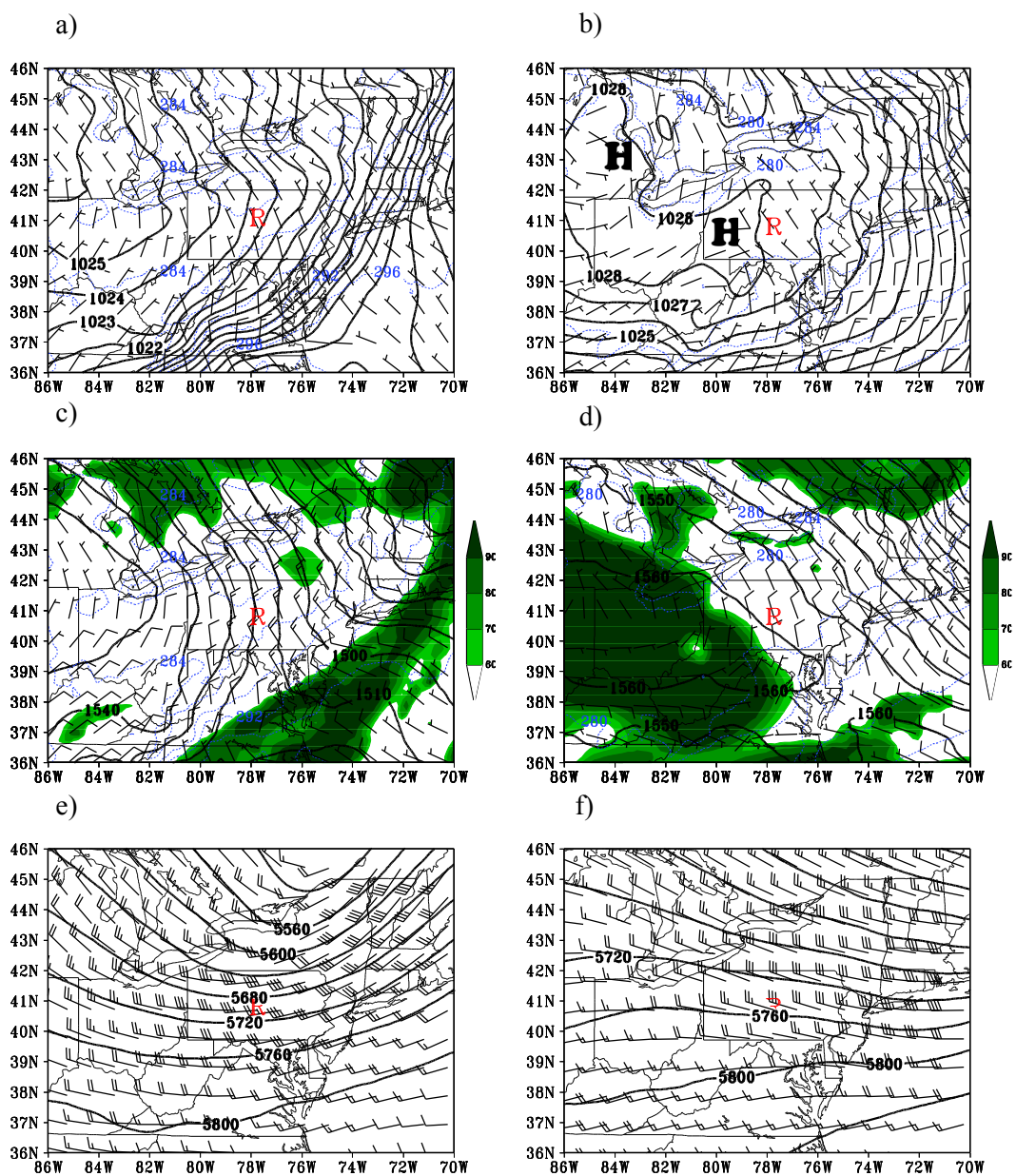
Figure 3-2. As Fig. 3-1, but for SEP16.

to 800 hPa by 1200 UTC. This directional shear maximum can contribute to the development of a ducting region and/or critical levels below 500 hPa and to the trapping of wave modes excited by the Allegheny Mts.

Overall, APR14 and SEP16 are characterized by weakening pressure gradients, clearing skies and weakening wind speeds. Both cases have wind directions with a westerly or west-northwesterly component perpendicular to the Allegheny Mts. and stability profiles that can support the development terrain-induced gravity waves. These cases also show strong directional shear between the surface and 500 hPa that can contribute to the development of critical levels and the trapping of gravity wave energy within this layer. Trapped wave can be expected to propagate southeastward and potentially impact the Rock Springs measurements. Evidence of such interactions is provided using network measurements in the following section.

3.1.2 Network Observations

Time series of 12-min center-averaged temperature, wind speed, wind direction, *Rib*, vertical heat flux and *TKE* for APR14 are provided in Fig. 3-3 (a-f). This case is characterized by near-neutral stability near the surface during the first 5 h of the night. This early period has weak surface cooling due to the presence of low level clouds and 1-6 m s^{-1} wind speeds. The weak stability coupled with large wind speed shear between 2 and 9 m results in Ri_b near 0 and *TKE* ranging from 0.2 to 0.8 m^2 s^{-2} before 0500 UTC. After 0500 UTC under clearing skies, strong near-surface stratification develops, and wind direction becomes highly variable throughout the network as the 2- and 9-m-AGL wind speed decreases below 1 m s^{-1}. Sudden shifts of wind direction from S to NW and back to S are accompanied by 1-1.5 K temperature fluctuations from 0600-0800 UTC at 2 and 9 m AGL. During this period, the Ri_b fluctuates to less than 1; heat fluxes are generally negative but fluctuate to positive values (associated with convective instabilities) with small, nonzero *TKE* values. It is important to note that these fluctuations are

found at all the sites throughout the observing network with various amplitudes (Fig. 3-4). Sites

located at lower elevation and thus deeper within the cold pool (e.g., Sites 8 and 12) experience
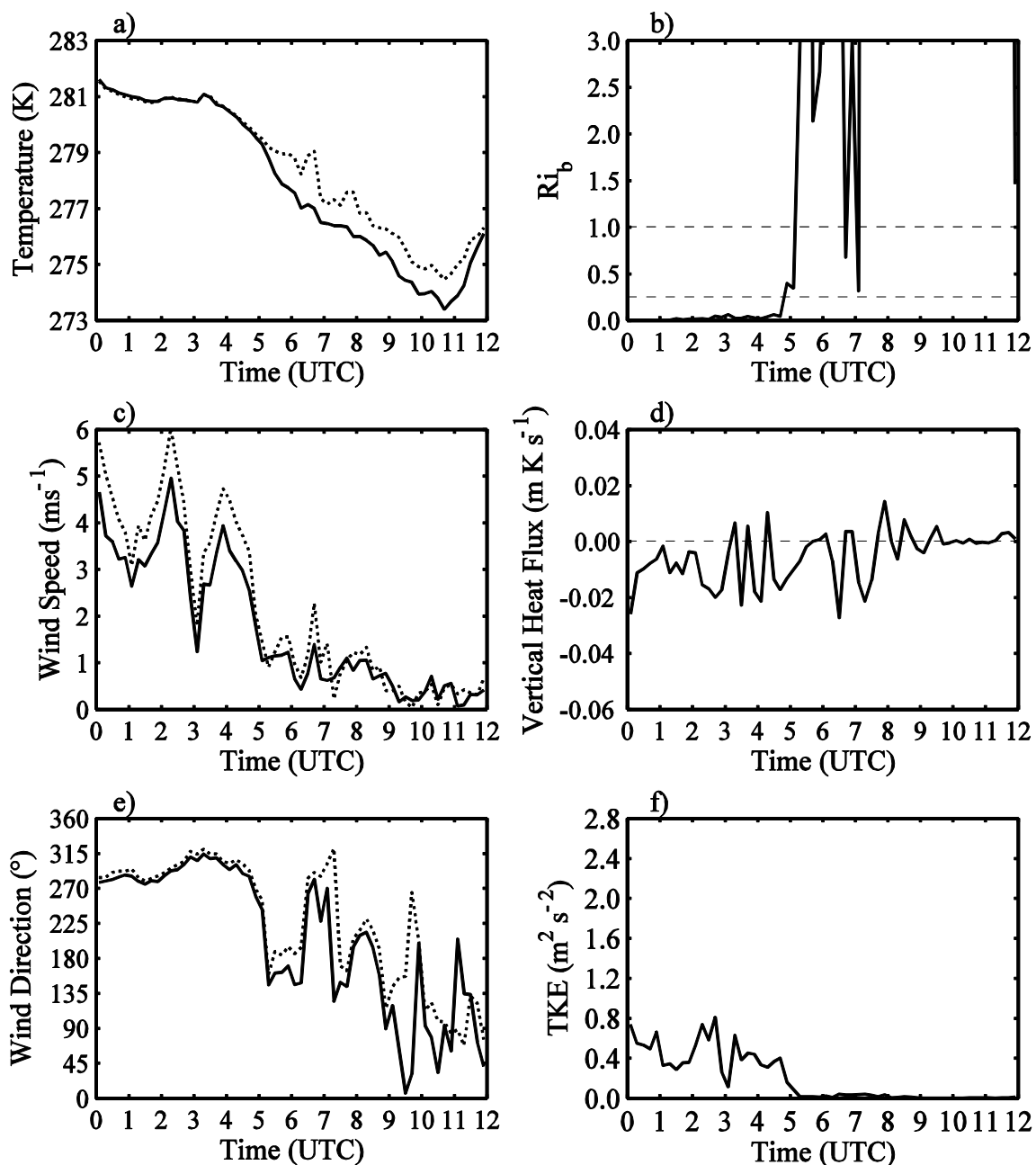
Figure 3-3. Time series at Site 9 of 12-min center-averaged temperature (a), wind speed (b) and wind direction (e) at 2 m (solid) and 9 m (dotted) AGL, *Rib* (b) and 2-m vertical heat flux (d) and *TKE* (f) for APR14 are presented.

temperature fluctuations ranging from 1-1.5 K, while sites located on the slopes (e.g., Site 6) experience temperature fluctuations less than 1 K.

These observations are supported by SODAR measurements. SODAR 2027, located on the slopes of Tussey Ridge for this case study, measures decreasing wind speeds after 0500 UTC from 30 to 180 m AGL (Fig. 3-5a). This period is characterized by variable westerly and northwesterly wind directions, roughly perpendicular to the ridge. From 0530 to 0630 UTC, the 30 to 150 m AGL layer is characterized by highly variable wind directions and directional shear. Note that at 0600 UTC wind directions vary from southwesterly to northerly between 40 m and 130 m AGL. The veering wind pattern suggests the presence of a short-lived circulation over the observing site. Between 0620 and 0640 UTC winds become northerly to north-northwesterly. This period is associated with stronger wind speeds that persist until 0730 UTC. During this
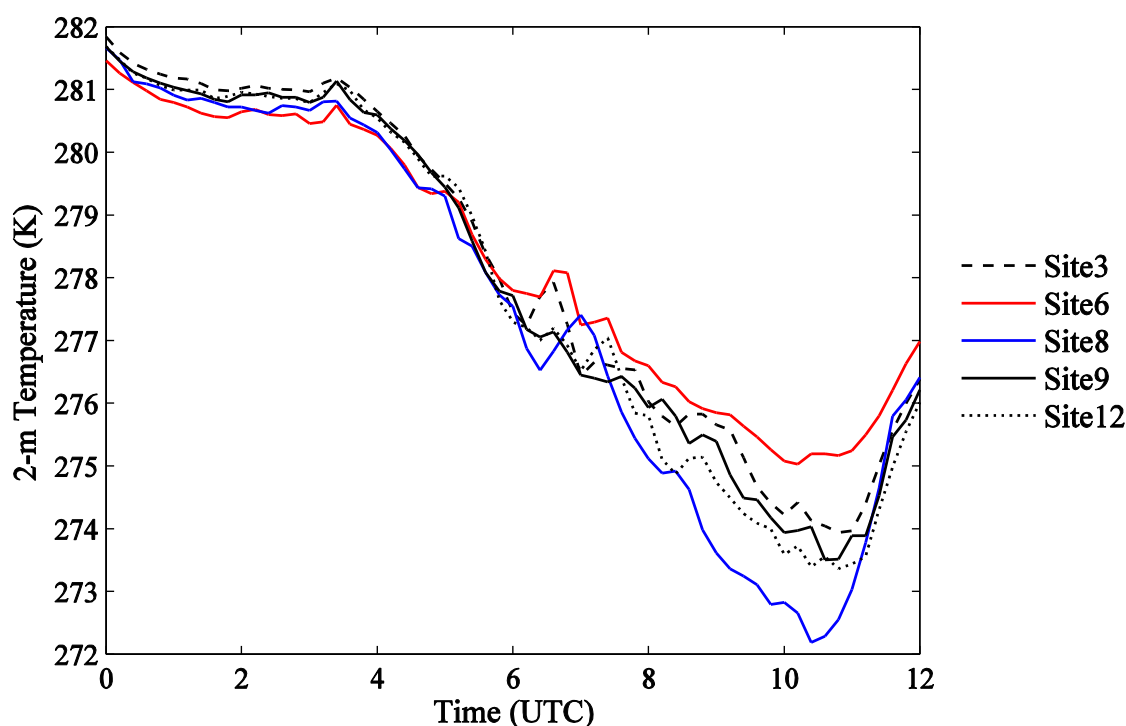
Figure 3-4. Time series of 12-min center-averaged 2-m temperature for multiple sites throughout the network during the APR14 case study suggest the presence of a horizontally coherent structure propagating away from Tussey Ridge between 0600 and 0800 UTC.

event, vertical motions are initially near 0 from 30 to 180 m, and become positive at 0.5 m s^{-1} from 0700 to 0730 UTC from 30 to 120 m AGL (Fig. 3-5b). This period is also characterized by weak but measureable *TKE*.

It is hypothesized that after the transition from near neutral conditions to strongly stable
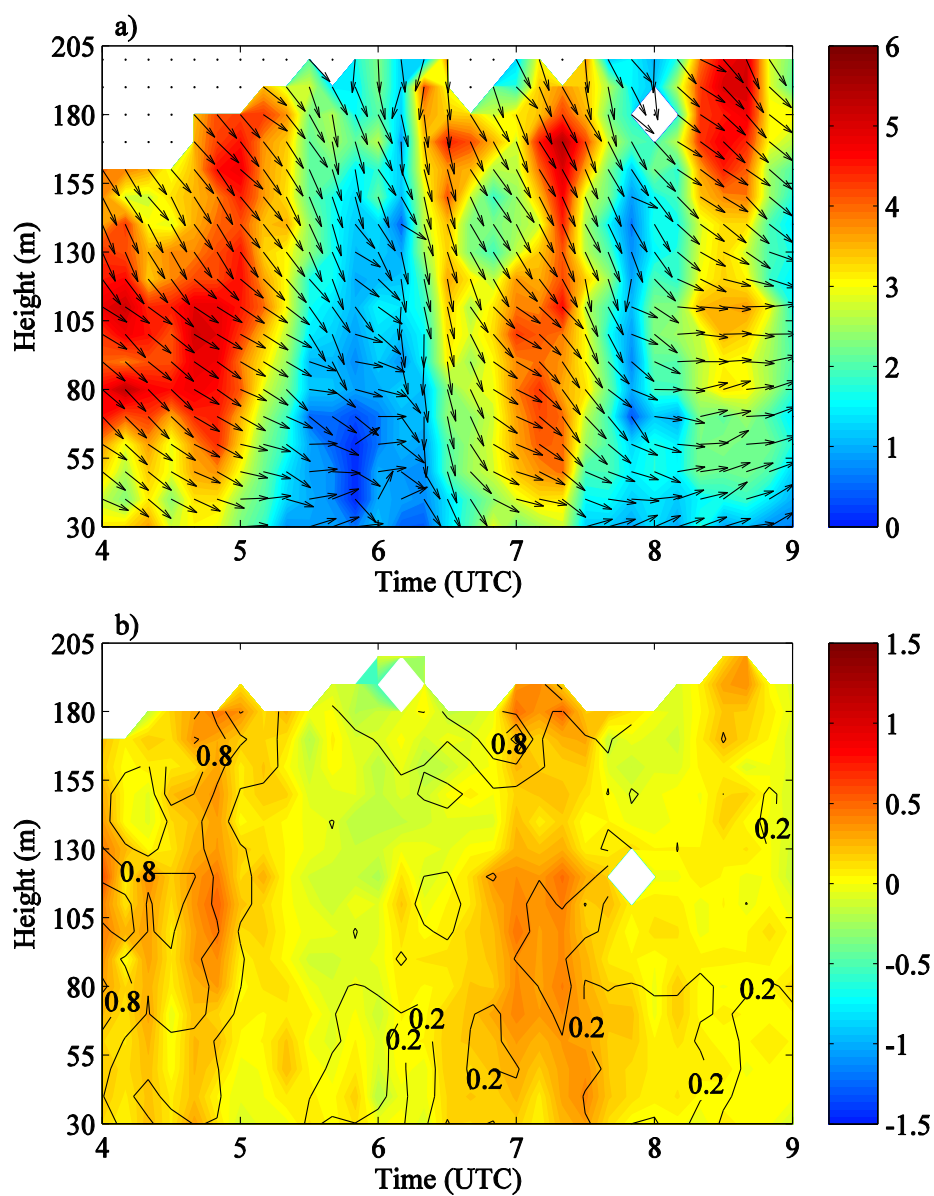
Figure 3-5. SODAR-derived (a) wind speed (m s^{-1}, shaded according to scale on right) and wind direction (arrow) and (b) vertical wind velocities (m s^{-1}, shaded according to scale on rigth) and *TKE* from 0400-0900 UTC APR14.

conditions, a rotor-like circulation develops over the network. This circulation is expected to have horizontal scales larger than 1 km and to extend parallel to the ridge for more than 3 km (as all the sites within the network experience the associated wind directional shifts and temperature fluctuations associated with it). The speed shear associated with the circulation acts to destabilize the atmosphere, reducing the Ri_b and producing convective instability associated with positive heat fluxes. This phenomenon is suspected to be short-lived over the observing stations producing fluctuations that last approximately 20 min. The directional shifts and temperature fluctuations are consistent with those associated with resonant lee waves producing a Type 1 rotor; since these fluctuations are accompanied by weak *TKE*.

The SEP16 case study shows temperature and wind fluctuations similar to those observed for APR14. This case is characterized by strong static stability, 2- and 9-m AGL wind speeds often less than 1 m s^{-1}, and highly variable wind directions (Fig. 3-6a, c, and e). SEP16 presents strong cooling during the first 6 h of the night followed by a 3-K temperature fluctuation at 2 and 9 m AGL between 0600 and 0900 UTC. During this period, the wind directions vary from southwesterly to easterly to northwesterly, and Ri_b is reduced to less than 1 on multiple occasions. There is measurable *TKE* at 2 m AGL and positive vertical heat fluxes associated with buoyant production of *TKE* due to convective instabilities during the times when the Ri_b is reduced (Fig. 3-6 d and e). This case also shows horizontally coherent temperature fluctuations (Fig. 3-7). Site 6 experiences the smallest temperature fluctuations from 0600-0900 UTC. The other sites located deeper within the cold pool experience larger amplitude fluctuations. There appears to be large spatial and temporal correlation between sites 3, 7, 8, 9, and 12. That is, they have similar initial warming time, rate of warming/cooling and timing of maximum warming, suggesting the presence of a feature that extends more than 0.8 km from the base of Tussey Ridge and extends more than 2 km along the valley and impacts almost all of the network sites simultaneously. The wavelength of the disturbance increases over time, encompassing site 6 by

0700 UTC. Thus, this event could be associated with a period of wave amplification and/or wavelength lengthening.

SODAR observations support the existence of a rotor-like circulation from 0600 to 0800
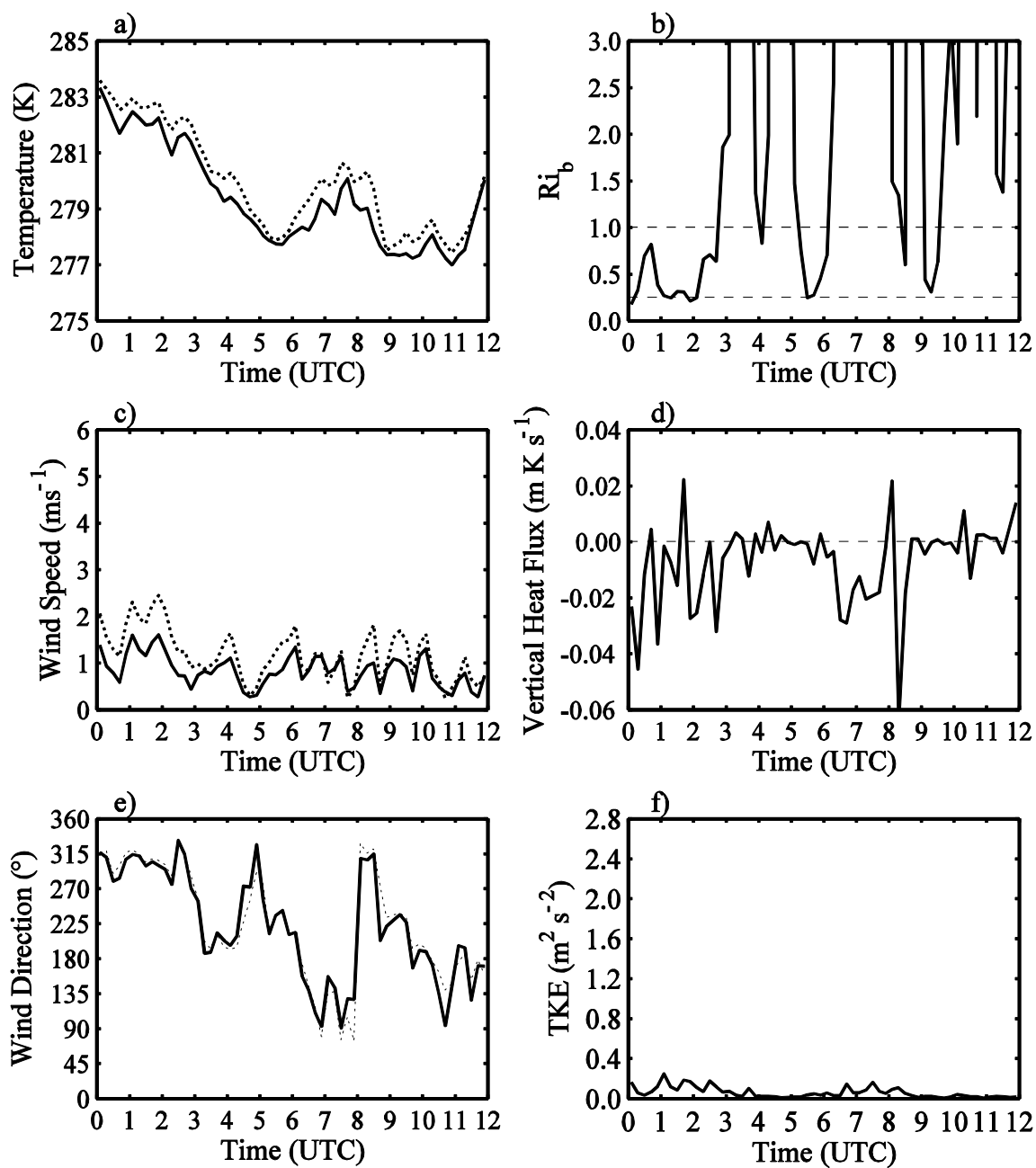
Figure 3-6. Same as Fig. 3-3 but for SEP16
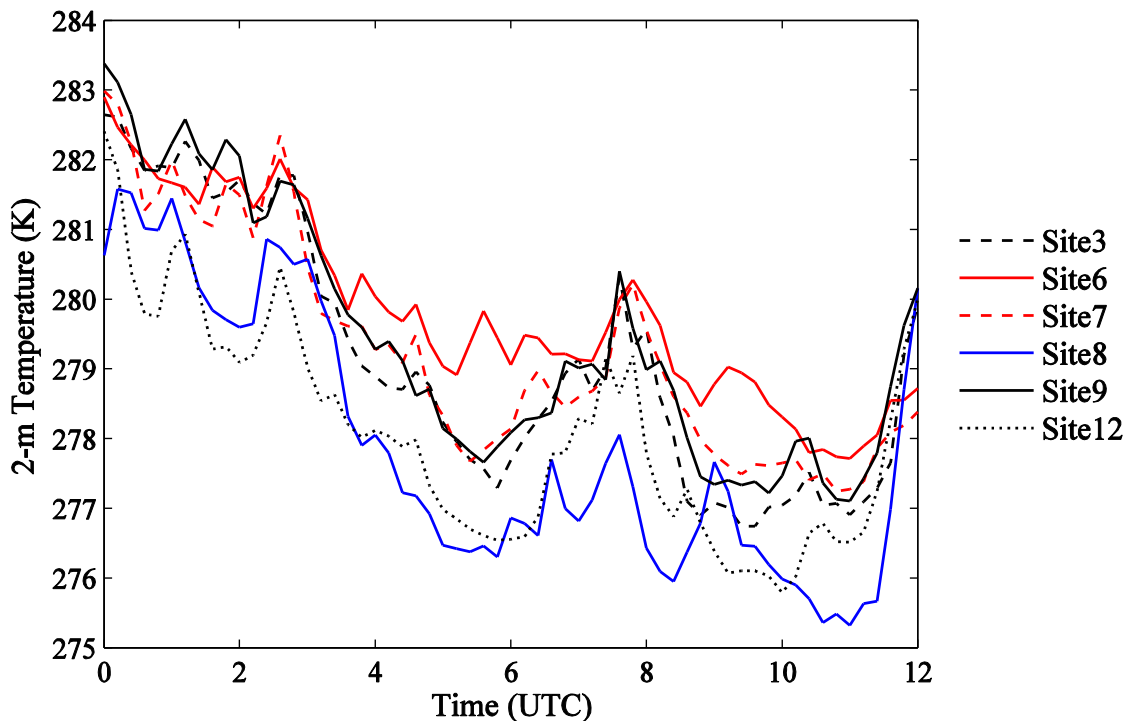
Figure 3-7. Time series for SEP16 of 12-min centered-averaged 2-m temperature for multiple sites within the Rock Springs network.

UTC near the base of Tussey Ridge. The SODAR wind speeds after 0630 UTC are generally less than 2 m s^{-1} extending from 30 m to 160 m AGL (Fig. 3-8a). A distinct wind reversal region, characterized by easterly flow and extending up to 115 m AGL where the center of the circulation is located, can be noted between 0700 and 0800 UTC. From 0720 to 0730 UTC, the center of the circulation is displaced upwards from 115 m to above 160 m AGL. After 0730 UTC, the depth of the reversal region steadily decreases down to 100 m AGL until 0810 UTC. No reversal flow can be identified after this period. The nighttime period is primarily dominated by weakly positive vertical motions ranging from 0 to 0.5 m s^{-1}. However, the onset of the reversal region is associated with downward vertical wind motions exceeding 1 m s^{-1} and extending from 30 to 155 m AGL and the generation of strong turbulent motions (Fig. 3-8b). A secondary burst of downward motion greater than 0.5 m s^{-1} and enhanced *TKE* generation is present between 0730

and 0740 UTC. This event corresponds to the maximum warming observed at multiple sites throughout the network and the maximum elevation of the amplifying circulation.

As with APR14, it is hypothesized that the presence of the resonant lee waves excited by
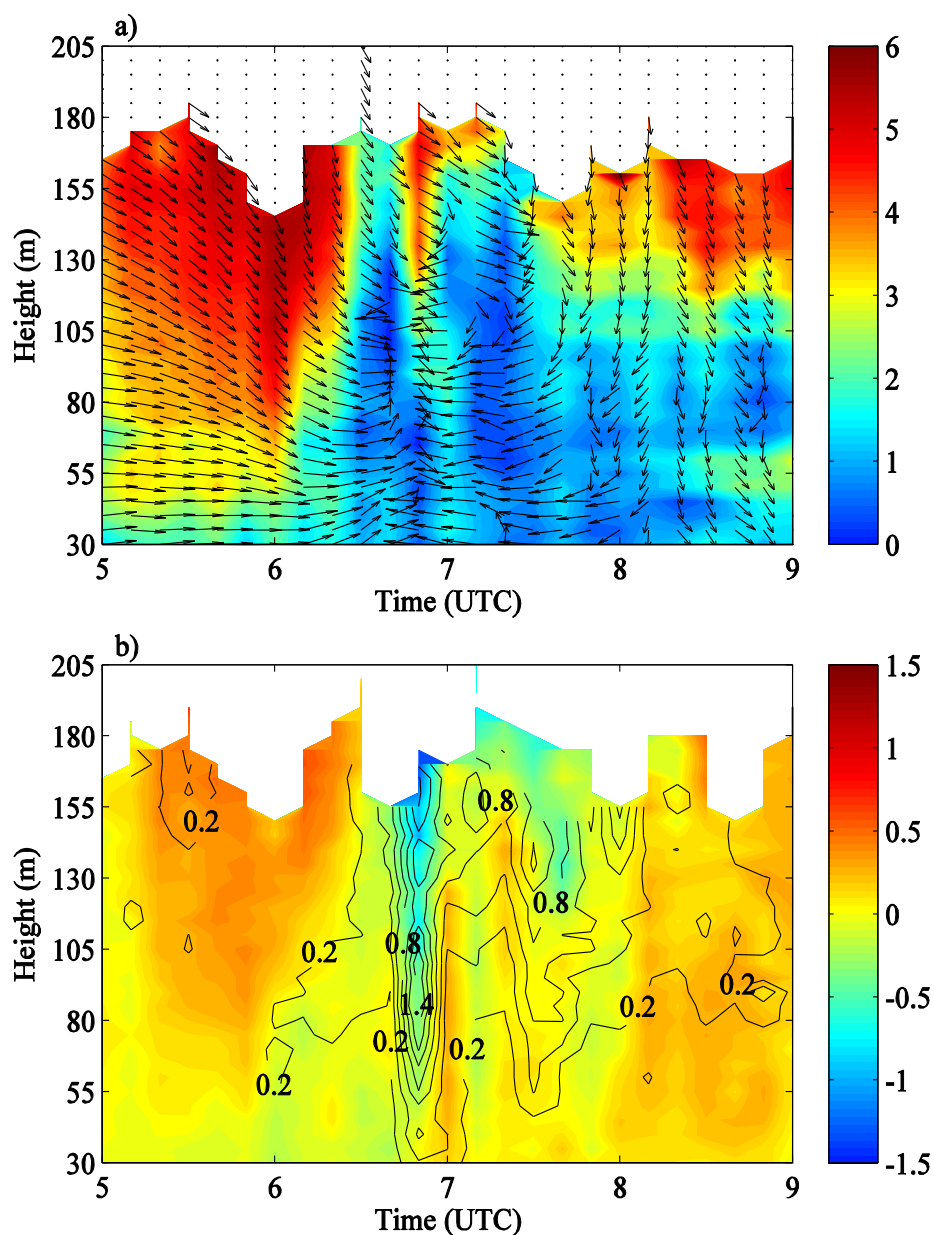
Figure 3-8. Same as Fig. 3-5. SODAR measurements from 0500-0900 UTC for SEP16 suggest the presence of rotor-like circulation between 0630-0800 UTC with a wind reversal regions extending up to 155 m AGL.

the Allegheny Mts. aid the development of a Type 1 rotor that amplifies and weakens between 0600 to 0800 UTC over the network. The speed shear associated with the rotor impacts the temperature structure, reducing the stability and Ri_b and enhancing TKE production.   The presence of this circulation impacts network observations over a 3-h period.   In addition, the cross-sectional dimension of this circulation is presumed to be larger than 1 km since its effects can be noted simultaneously at all sites within the network.

Overall, the APR14 and SEP16 cases produce temperature, wind speed and wind direction fluctuations that suggest the presence of Type 1 rotor circulations associated with resonant lee waves excited by the Allegheny Mts. Temperature fluctuations in both cases appear to be associated with regions of temporal wind direction variations of up to 90º and 180º (for APR14 and SEP16 respectively), wind speeds less than 1.5 m s^{-1}, and enhanced TKE generation extending from the surface up to 160 m AGL. These circulations act to reduce the local Ri_b and increase TKE. Wave breaking may be occurring due to the presence of convective instabilities as noted by the positive vertical heat fluxes during the periods when the rotor circulation is hypothesized.

3.2 Resonant Lee Waves Excited by Tussey Ridge: NOV06 and DEC04

NOV06 and DEC04 are characterized by southerly flow and strong static stability over Central PA. Both cases are suspected of producing gravity waves that are excited by Tussey Ridge and impact the Rock Springs observing network throughout the night.   In this section, synoptic conditions and Rock Springs network observations are presented in order to further investigate the origin of these motions.

3.2.1 Synoptic Conditions

NOV06 is characterized by low-level strong stratifications, weak wind speeds, and large directional shear through most of the night (Fig. 3-9a-f). The 500-hPa flow is driven by the presence of a high pressure system over the Georgia-Tennessee border (not shown) that slowly moves eastward over the 12-h nighttime period. At this level, the flow over Central PA is weak (~10 m s^{-1}) and from the northwest through most of the night (Fig. 3-9 e and f). The 850-hPa high pressure system is located over southern PA and northern Maryland. Through the night, the system moves off the East Coast and into the western Atlantic as mid-level wind directions change from southerly to southwesterly through the nighttime period (Fig. 3-6 c, d). Increasing pressure gradients below 850 hPa results in wind speed increasing from 5 m s^{-1} at 0000 UTC to 10 m s^{-1} at 1200 UTC. The surface high pressure system is located over eastern PA and northern Virginia at 0000 UTC and moves offshore by 1200 UTC. Wind speeds are less than 5 m s^{-1} near the surface and wind directions vary from south-easterly to southerly through the nighttime period. Overall, this case is characterized by very weak winds near the surface and clear skies. KUNV reports clear skies and calm wind speeds of less than 2.6 m s^{-1} through the entire night.

This case, characterized by strong stratification due to the absence of clouds, weak synoptic pressure gradients, and weak winds, shows strong directional shear (nearly 180º) from the surface to 500 hPa. Since wind directions near the surface are predominantly southeasterly through most of the night, this implies a cross-mountain flow that can potentially excite wave motions from Tussey Ridge. At 850 hPa however, the flow transitions from southerly to southwesterly between 0000-1200 UTC, where by 500 hPa, the flow is primarily northwesterly. This suggests the development of numerous critical levels throughout the night that can trap wave motions. Both NARR and the KPIT sounding from 0000-1200 UTC suggest a decrease in elevation of the directional wind shear maximum. By 1200 UTC, wave motions excited by the terrain can be expected to be trapped below 850 hPa since the wind speed component perpendicular to the mountain vanishes below this level. Thus, the trapping of wave motions near

the surface become likely.

DEC04 is characterized by a westerly wind component at 500 hPa (Fig. 3-10e and f). This case features a 500-hPa ridge over eastern USA and wind speed of 10-15 m s^{-1} over Central PA through most of the night. At 850 hPa, a high pressure system, located over the East Coast at
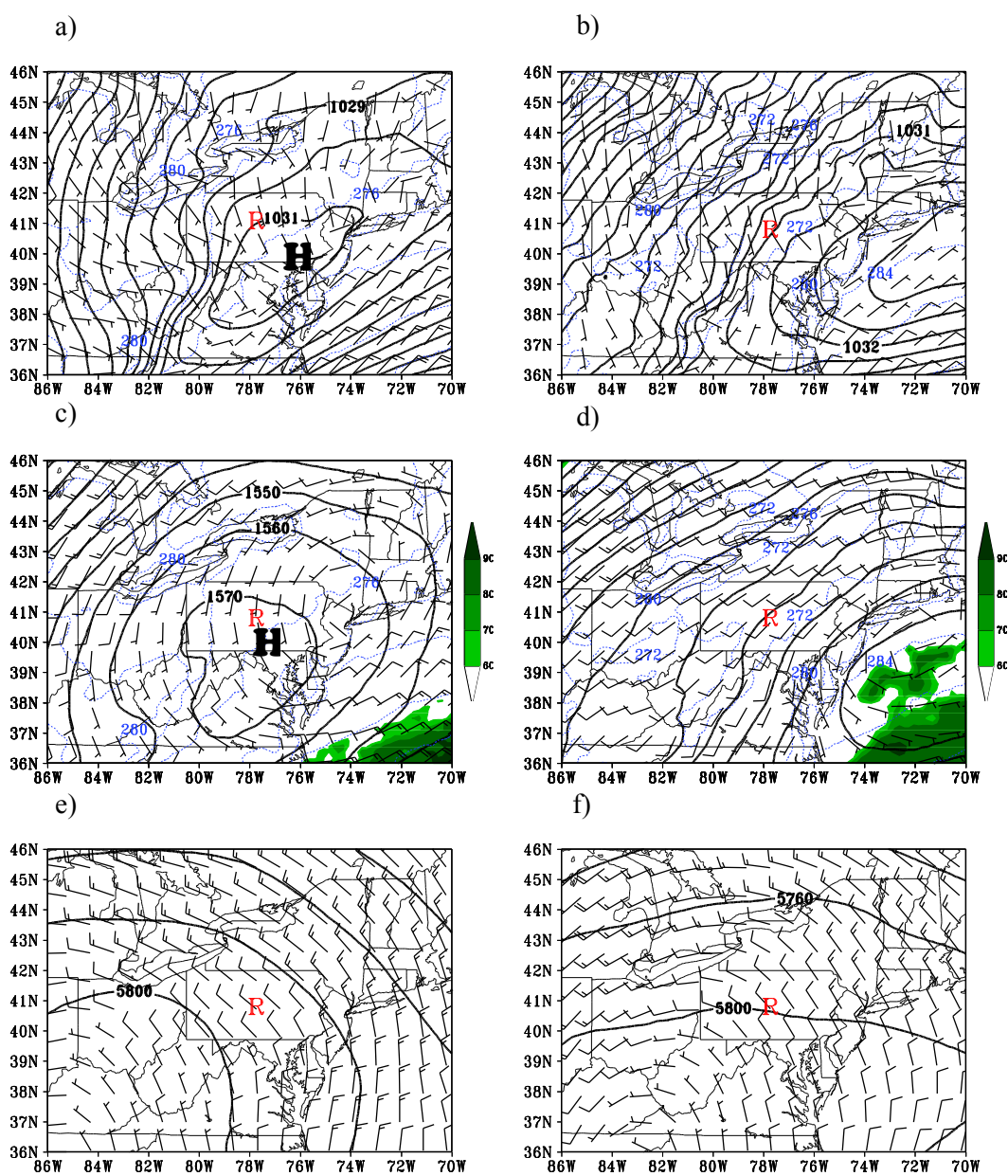
Figure 3-9. As Fig. 3-1 but for NOV06.

0000 UTC, induces a mostly south-southwesterly flow with 10-m s^{-1} wind speeds over Central

PA (Fig. 3-10c and d).   As the high pressure system moves eastward, increasing pressure

gradients associated with a low pressure system over Lake Ontario (not shown) result in stronger

wind speeds (15-20 m s^{-1}) over Central PA. At the surface, the flow remains predominantly weak

(~ 5 m s^{-1}) and from the south-southeast (Fig. 3-10 a, b). Skies remain clear over Central PA
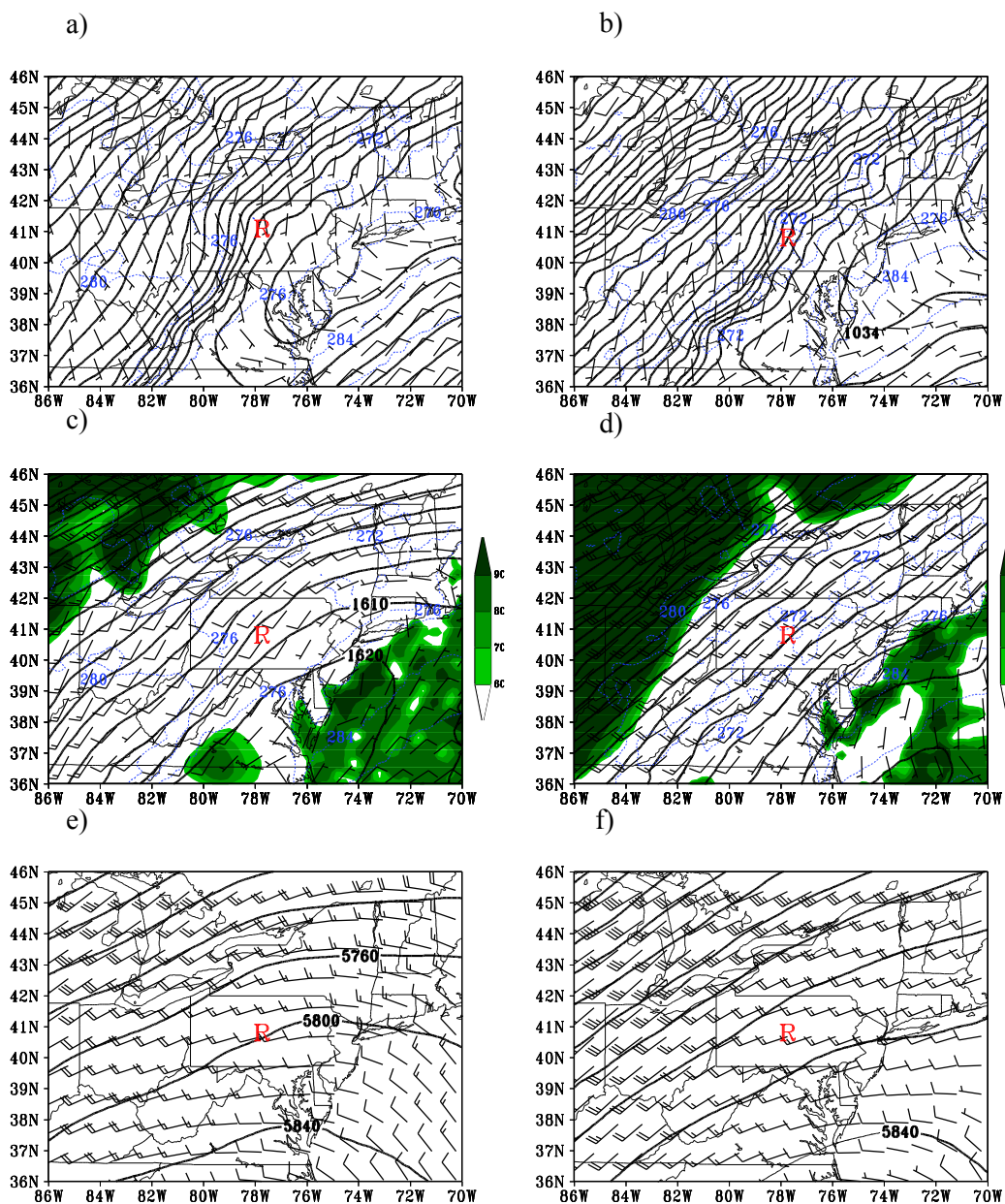
Figure 3-10. Same as Fig. 3-1. NARR reanalysis for DEC04.

throughout the night.

Like NOV06, DEC04 is characterized by strong stratification near the surface due to weak wind speeds and the lack of cloud coverage. However, this case features nearly 90º directional shear from the surface to 850 hPa through the 12-h nighttime period. The component perpendicular to the mountain vanishes by 850 hPa, suggesting the presence of a critical level and trapping of wave energy below this level. The presence of this trapping region persists through the night; thus wave activity generated by Tussey Ridge is likely present.

Overall, both cases are characterized by high pressure systems over the East Coast. These systems induce a mostly southerly flow over Central PA near the surface. Both cases exhibit directional shear of up to 90º between the surface and 850 hPa. In both cases, the wind component perpendicular to the mountain vanishes near 850 hPa throughout the night suggesting the presence of a critical level. Thus, trapped wave motions, excited by Tussey Ridge, are hypothesized to be important in these cases.

3.2.2 Network Observations

Observational evidence for the presence of wave-turbulence interactions due to the presence of gravity waves excited by Tussey Ridge over the Rock Springs network is presented for the two cases: NOV06 and DEC04. NOV06 is the more stable of the two. This case is characterized by very weak cooling throughout the night and strong stratification (up to 0.3 K m^{-1} or 2 K over 7 m) between 2 and 9 m AGL (Fig. 3-11a). The 2-m temperature is roughly 276 K with fluctuations of up to 2 K appearing through most of the night. Weak wind speeds of less than 1 m s^{-1} and highly variable wind directions are also observed during this case study (Fig. 3-11c and e). Wind speed fluctuations greater than 1 m s^{-1} are associated with the largest temperature fluctuations and wind direction shifts from of 90 to 180º at 2 and 9 m AGL. Due to the strong stratification and very weak wind speed, the Ri_b is generally above 1, except during a

period between 0430 and 0500 UTC (Fig. 3-11b). This period is associated with a 1 K 2-m temperature fluctuation, reduced stability through the 2-9 m AGL layer and a wind speed maximum of 1.5 m s^{-1}. Despite very positive Ri_b, positive vertical heat fluxes and TKE of up to
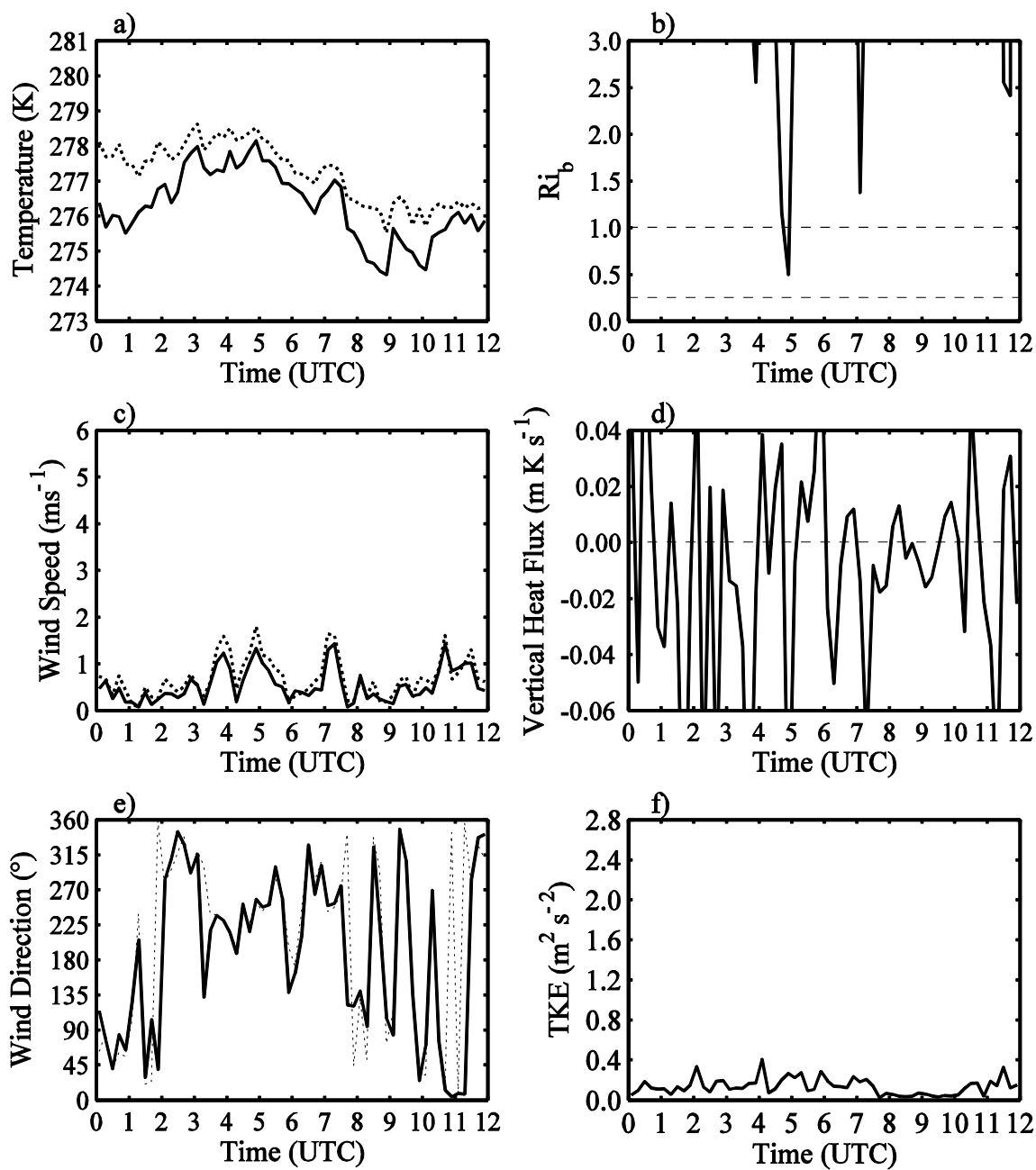
Figure 3-11. As in Fig. 3-3 but for NOV06.
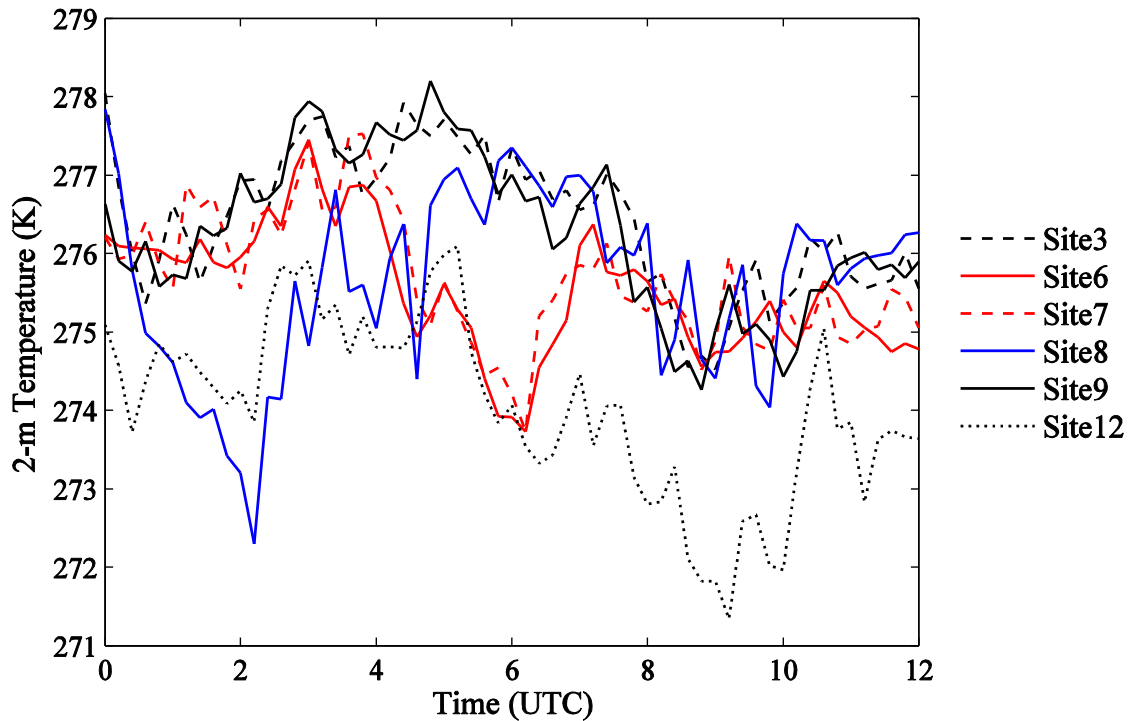
Figure 3-12. Time series of 12-min, centered-averaged, 2-m temperature for multiple sites show large temperature fluctuations (up to 4 K) in the sites higher up in Tussey Ridge's slopes (Sites 6 and 7) and located lower within the cold pool (Sites 8 and 12).

0.4 m2 s-2 are observed at times during the night (Fig. 3-11d and f). This is one of the cases where the local Ri_b is not an adequate parameter to quantify the presence of turbulence in the SBL.

Large temperature fluctuations are observed at various sites through the network (Fig. 3-12). For this case, Sites 3 and 9 present the smaller fluctuations compared to Sites 6, 7, 8, and 12. Sites 3 and 9 however show a ~2 K increase in 2-m temperature for 0000-0430 UTC despite the absence of cloud coverage and weak wind speed and mixing; while site 8 (furthest from the ridge) experiences a 5.5 K cooling from 0000-0200 UTC. Sites 6 and 7 show a temperature drop of 3 K from 0330 to 0600 UTC followed by a 2 K temperature increase. Both of these sites are located further up the slopes of Tussey Ridge, where lee-wave motions in this case are hypothesized to have a greater impact. Sites 8 and 12, located lower within the cool pool, experience large

temperature fluctuations of up to 4 K throughout the night. Despite having lower temperatures, the 2-m temperature time series at Site 12 show strong correlations to those observed at Sites 3 and 9, but with larger amplitude fluctuations. There appears to be weak spatial coherence between the network sites before 0700 UTC. Site 3, 6, 7, and 9 appear to be somewhat correlated, experiencing similar warming rates from 0000-0300 UTC. However after 0330 UTC, sites 6 and 7 appear to no longer be affected by the mechanism responsible for the warming, and thus cool 3 K by 0600 UTC. Sites 3 and 9 appear to be impacted by the warming mechanism until 0500 UTC, after which they begin to slowly cool. After 0700 UTC all of the sites adjacent to the mountain, with the exception of Site 12 (located at the lowest elevation and thus deeper within the cold pool), exhibit similar temperature fluctuations. This might suggest that sites 3, 6, 7, and 9 are affected by a phenomenon with wavelength greater than 1 km through most of the night except between 0330 and 0700 UTC, when the wavelength of the phenomenon decreases or the location of the event is displaced away from the ridge.

SODAR 2027 measurements for this case suggest the presence of a rotor-like circulation over the network (Fig. 3-13a and b). It is important to note that during this event, SODAR 2027 is located lower within the valley near site 10 (approximately 0.9 km from site 9) This case exhibits weak vertical motions of less than 0.5 m s^{-1} through most the night from 30 to 105 m AGL. This layer is characterized by highly variable wind directions. Nevertheless, a predominantly easterly wind direction can be observed prior to 0200 UTC. After this period, a shallow reversal region characterized by southwesterly flow extends from 45 to 65 m AGL. The wind directions above this layer are predominantly from the east. The center of the circulation is located at approximately 70 m AGL between 0200 and 0400 UTC. At 0430 UTC, the wind speed peaks at 3 m s^{-1} and the wind becomes southwest through the lowest 105 m AGL. This period is hypothesized to be associated with the flow reversal region of a large rotor-like circulation and/or the displacement of a pre-existing circulation away from Tussey's slope due to wavelength
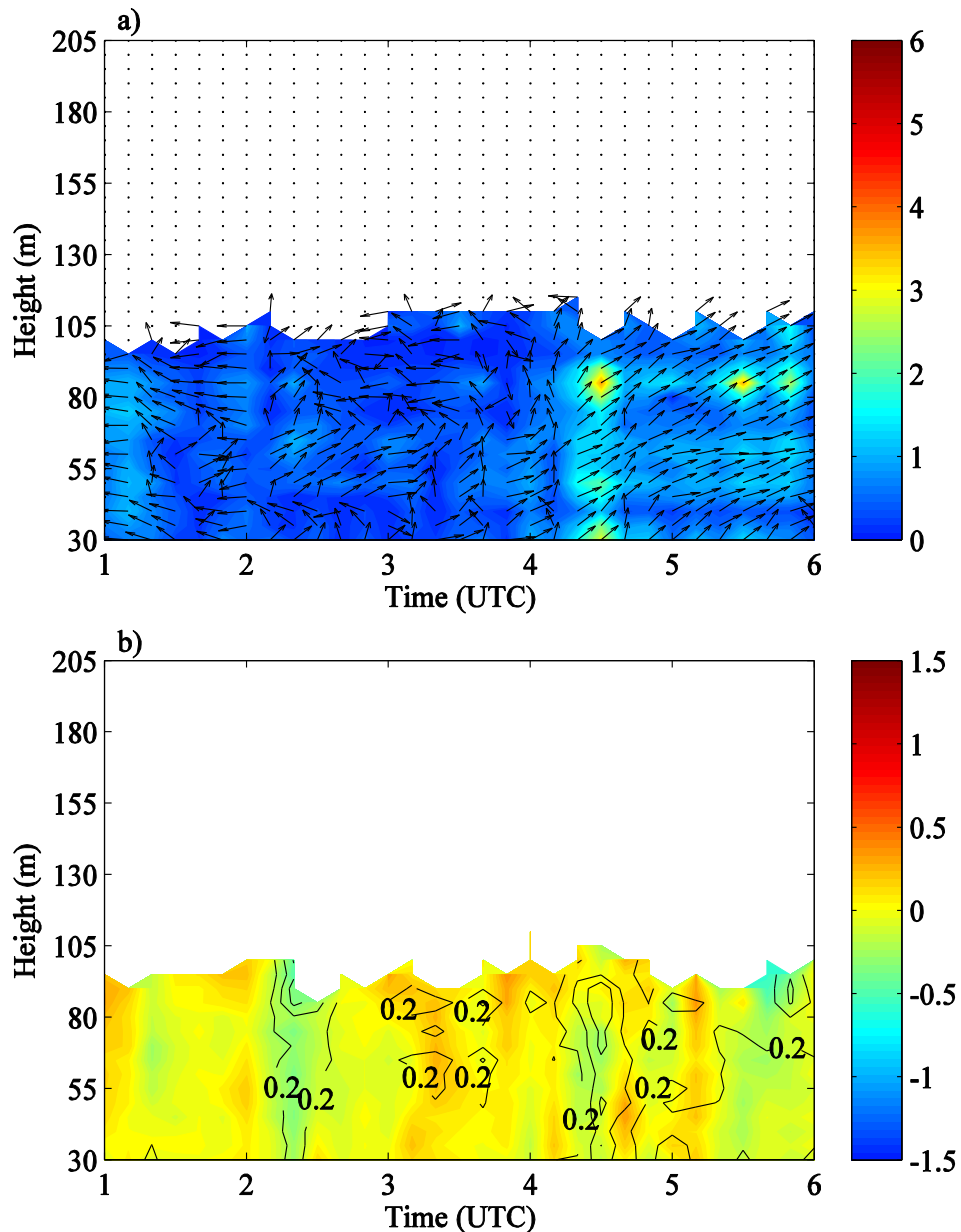
Figure 3-13. As in Fig. 3-5 but for 0100-0600 UTC for NOV06

lengthening. The onsets of the circulations at 0230 and 0430 UTC are marked by downward

vertical motions and enhanced *TKE* production (Fig. 3-13b). A region of *TKE*, higher than the

ambient, is produced from 100 m down to 30 m AGL. It is hypothesized that trapped lee waves

excited by Tussey Ridge induced and enhance a rotor-like circulation with varying wavelength

and/or location over the network. Rotor-like circulations act to enhance overturning, increase

turbulent mixing and transport higher potential temperature air from higher levels down to the surface resulting in the warming of the lower levels. Thus temperature, wind speed and wind direction fluctuations throughout the network appear to be related to changes in the background wind, descending motions and enhanced *TKE*.

DEC04 is characterized by very weak cooling at 2 and 9 m AGL throughout the night (Fig. 3-14a). However this case, characterized by very weak stratification and relatively strong wind speed, exhibits temperature fluctuations of approximately 0.5 K during the first few 5 hours of the night. These fluctuations appear to have 1-h period of oscillation and are accompanied by large amplitude wind speed fluctuations of 3-4 m s^{-1} and wind directional shifts of 90-180º (Fig. 3-14c and e). The brief periods between temperature fluctuations are associated with stronger stratification and weaker wind speeds; thus the Ri_b becomes highly positive (Fig. 3-14b). During the periods of reduced stability, the vertical heat flux becomes positive as convective instabilities develop (Fig. 3-14d). *TKE* minima are observed when the Ri_b reaches a local maxima, but large *TKE* values, up to 2.5 m2 s-2, are noted through the entire night despite Ri_b being greater than 1 during some periods.

The 2-h temperature fluctuations are observed at various sites within the network (Fig. 3-15). Sites 7, 9, and 12 experience less than 2 K of cooling throughout the night. However, site 8 appears to have the largest cooling of 2.5 K from 0000-0400 UTC. It is important to note that site 8 is located furthest from the Ridge and at lower elevation. Sites 7, 9, and 12 have strong spatial coherence since they have similar temperature variations throughout the night. Site 7 shows larger temperature fluctuations between 0100 and 0300 UTC than site 9 and 12.

SODAR 2027 appears to show a rotor-like circulation that persists through most of the DEC04 night (Fig. 3-16a and b) with very weak wind speeds of less than 1 m s^{-1} from 30 to 105 m AGL. SODAR-derived wind directions suggest the development of multiple rotor-like circulations with wind reversal regions of 180º from 0150 to 0600 UTC. During periods having

the rotor-like circulations, the near-surface flow is predominantly westerly, while the flow near 100 m AGL is predominantly easterly. The center of the circulations is located approximately 75 to 90 m AGL. The periods of largest directional shear are associated with fluctuations in vertical velocities of approximately 0.5 m s^{-1} and enhanced-*TKE*. The time periods from 0200-0240,
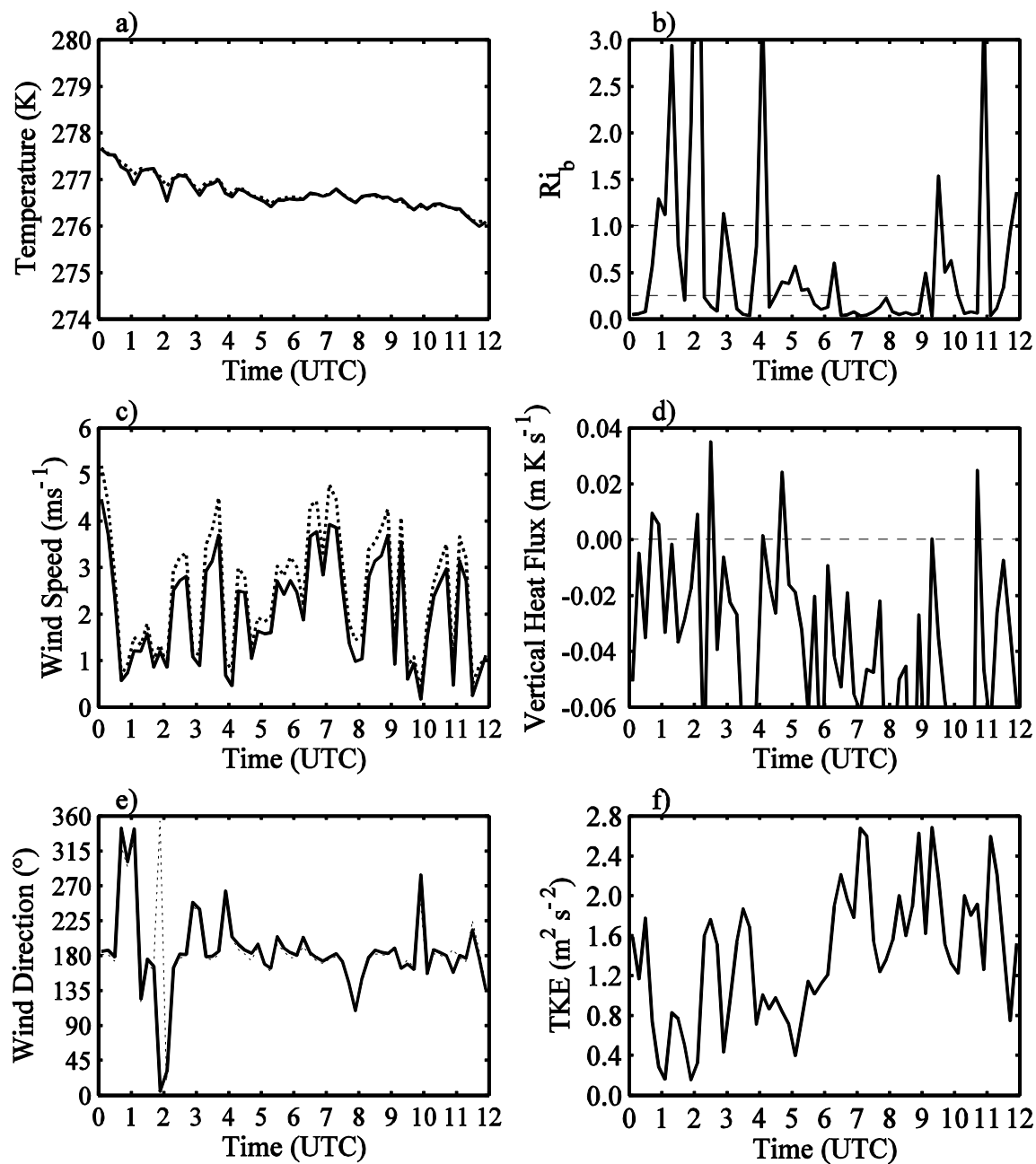
Figure 3-14. Same as Fig. 3-3 but for DEC04.

0320-0340, and 0420-0440 UTC show enhanced-*TKE* regions that extend from 90-105 m AGL down to 30 m AGL. These periods correspond to *TKE* maxima at 2 m AGL at Site 9 (~1 km away). This suggests there is strong spatial correlation between the sites and thus they are highly likely affected by the same phenomenon.

Despite different stratifications and wind speed, both cases exhibit little cooling throughout the night and wind direction fluctuations that suggest the presence of reversal flow regions due to gravity waves generated by Tussey Ridge. Limited spatial coherence within the network suggests the presence of phenomena with small wavelength and/or varying location. Rotor-like circulations with centers of circulations located between 70-90 m AGL are confirmed using SODAR measurements in both cases. SODAR measurements also confirm the existence of
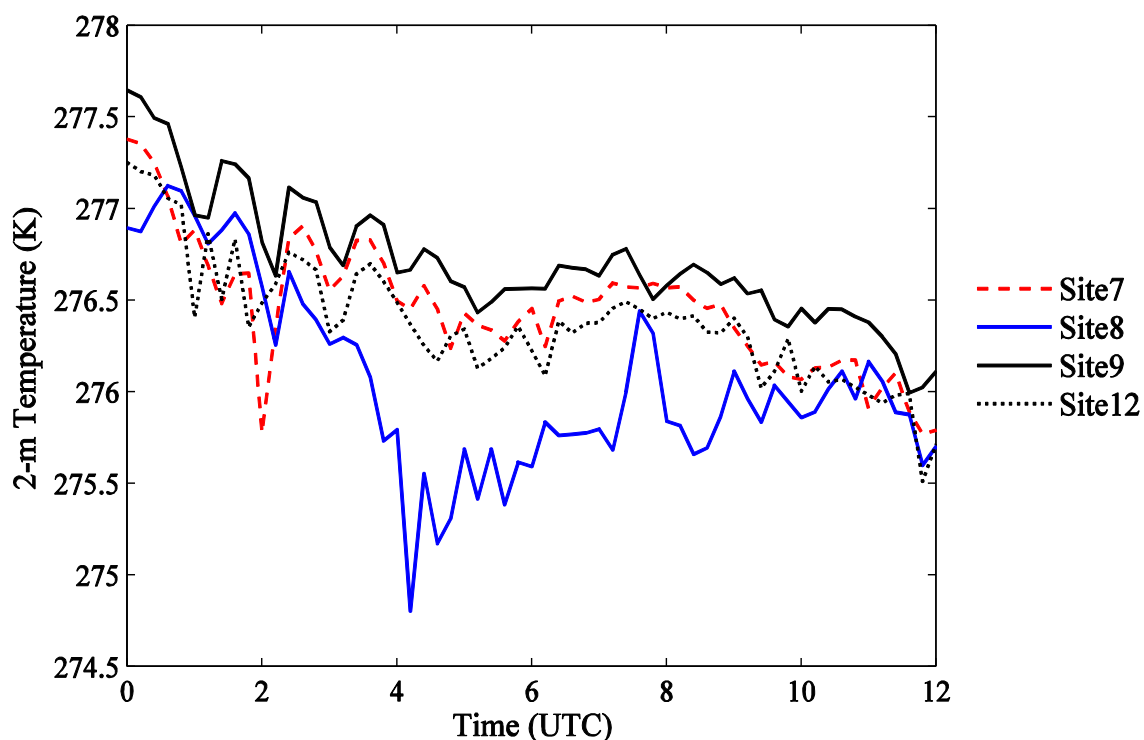
Figure 3-15. Time series of 12-min centered-averaged 2-m temperature for multiple sites on DEC04 show temperature fluctuations, less than 2 K, through the night. The fluctuations are largest at Site 7 (higher up the slopes) and Site 8 (lower within the cold pool).

enhanced *TKE* regions reaching 30 m AGL. The presence of rotor circulations acts to reduce the local stability, increase *TKE*, and contribute to wave breaking and the development of convective instabilities near the surface.
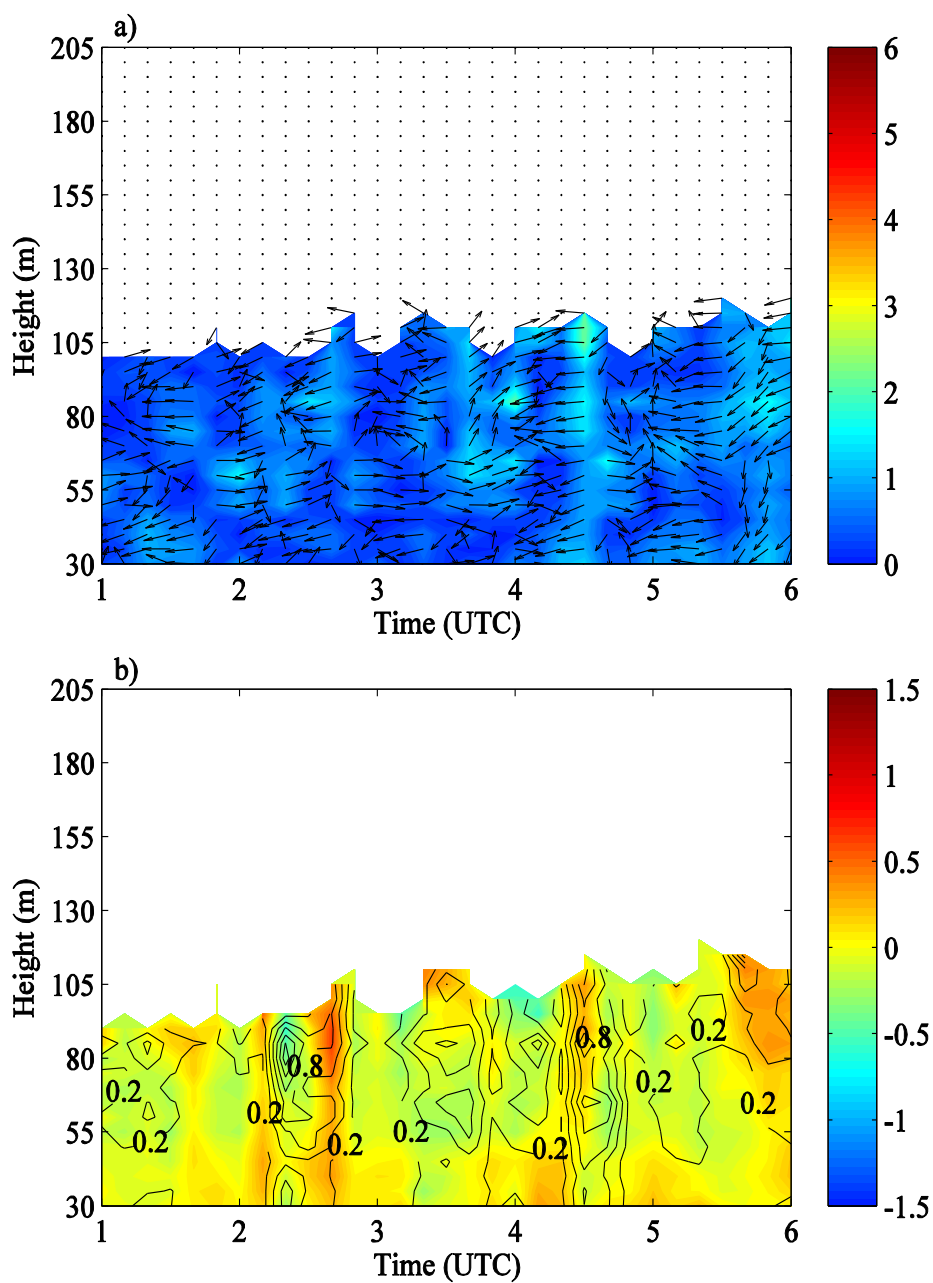
Figure 3-16. As in Fig. 3-5 but for 0100-0600 UTC for DEC04

3.3 Downslope Wind Events Generated by Tussey Ridge: AUG24 and NOV13

Two case studies reporting temperature and wind fluctuations resembling those of downslope wind storms are analyzed: AUG24 and NOV13. These cases are associated with large rapid warming and increasing wind speed over a short period, similar to those observed due to downslope windstorms. In this section, the synoptic conditions leading to the events and network observations are presented.

3.3.1 Synoptic Conditions

AUG24 is characterized by a westerly to southwesterly wind directions and increasing wind speeds from 5 to 15 m s^{-1} throughout the night over Central PA at 500 hPa (Fig. 3-17e and f). At 850 hPa, the flow is westerly to southwesterly and influenced by a weak ridge over Central PA at 0000 UTC (Fig. 3-17c and d). By 1200 UTC, the wind directions are predominantly southwesterly as a deep, low pressure system moves over the Great Lakes. The strengthening of the pressure gradients below 850 hPa result in wind speeds increasing from 5 to 10 m s^{-1} over Central PA through the 12-h nighttime period. At the surface, weak high pressure over eastern PA moves off the East Coast through the night (Fig. 3-17a and b). Over Central PA, the flow at 0000 UTC is south-southwesterly and less than 5 m s^{-1} and the flow remains weak and predominantly from the south through most of the night. KUNV reports very weak winds through most of the night and some scattered elevated clouds at 2-3 km at 0200, 0400 and 0700 UTC.

AUG24 features increasing directional shear from 45º to 90º in the lower atmosphere through the night. The cross-mountain wind component vanishes by 850 hPa; thus wave motions are constrained within this layer and trapping is very likely. In addition, NARR reanalysis and the Pittsburgh soundings suggest the development of an inversion at approximately 600 m ASL
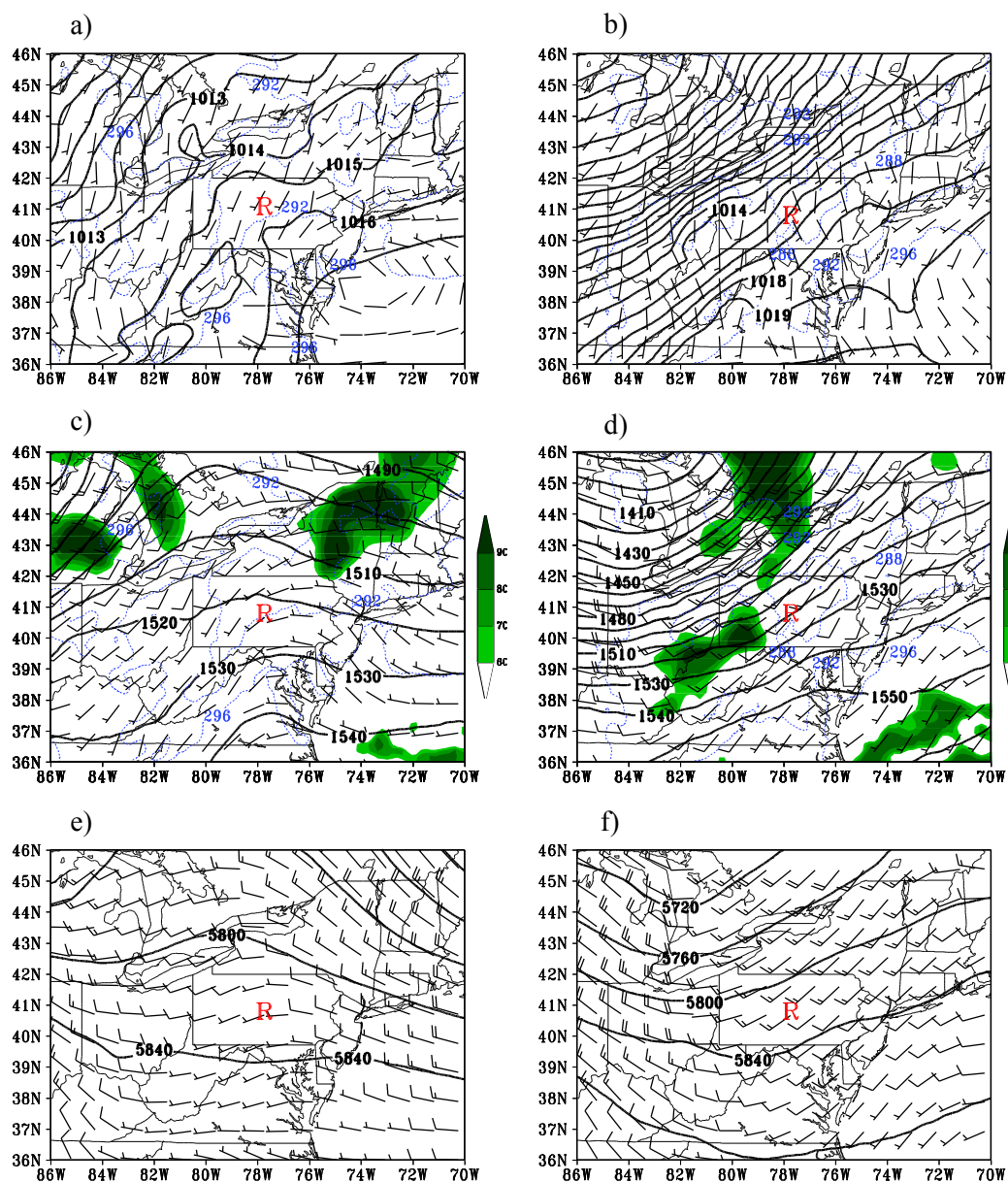
Figure 3-17. As in Fig. 3-1 but for AUG24.

(not shown). This would create a near-mountain top inversion for Tussey Ridge and possibly lead to a downslope windstorm-like event.

Finally, NOV13 is characterized by increasing pressure gradients over Central PA through the night (Fig. 3-18). The flow is predominantly westerly at 500 hPa at 0000 UTC and

southwesterly by 1200 UTC. However, tightening of geopotential heights is observed in this region as a strong low pressure system begins to move eastward over central Canada. This transition is accompanied by increasing wind speed from 15 to 25 m s^{-1} from 0000 to 1200 UTC. At 850 hPa, wind directions change from westerly to southwesterly, with increases in wind speed
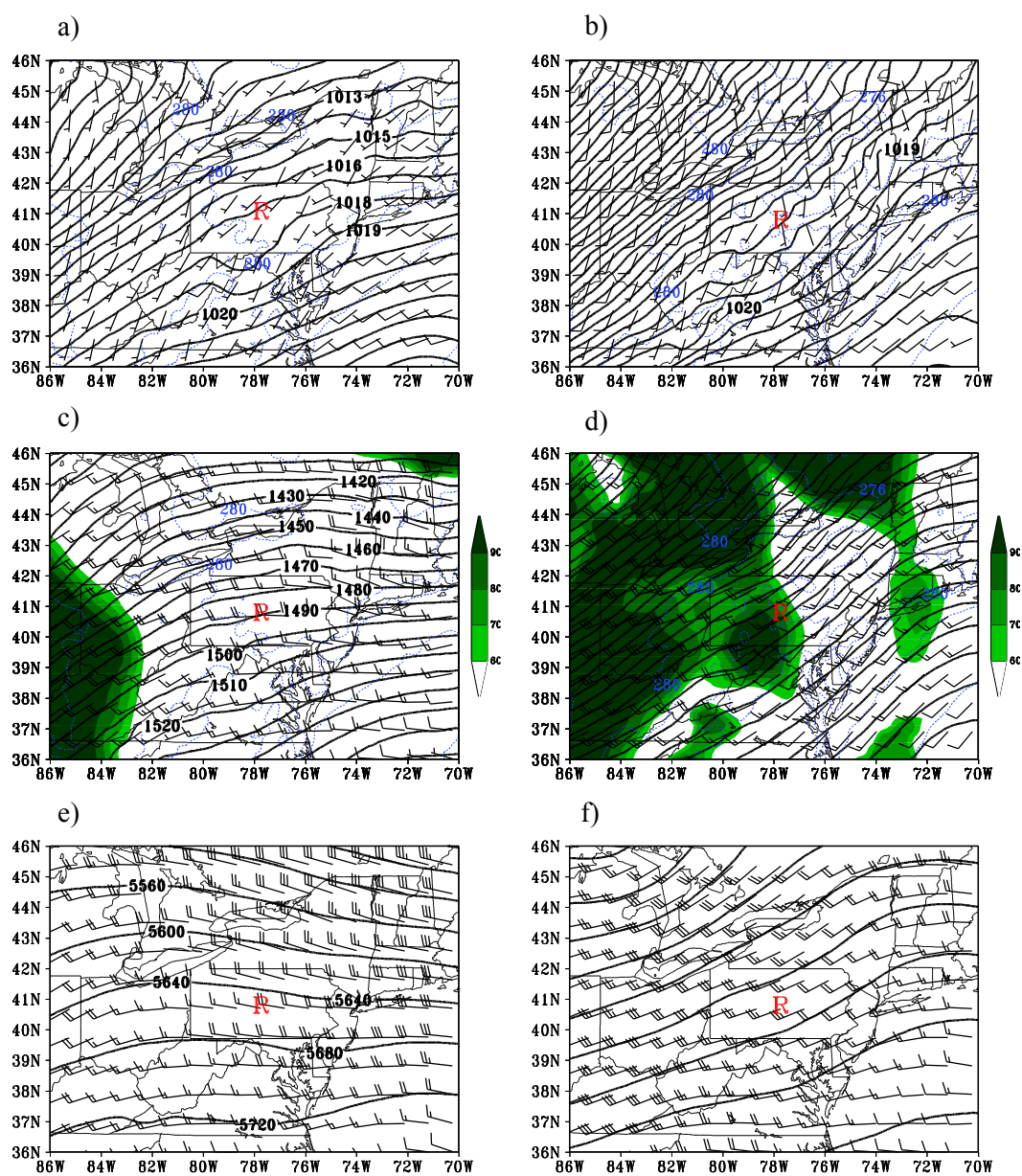
Figure 3-18. Same as Fig. 3-1. NARR reanalysis for NOV13.

from 20 to 25 m s^{-1} over Central PA (Fig. 3-18c and d). At the surface, the wind direction is primarily from the south through the night with wind speed increasing from 5 m s^{-1} to 10 m s^{-1} (Fig. 3-18a and b). This case is characterized by clear skies through most of the night.

NOV13 features weak (<45°) directional shear and strong speed shear between the surface and 850 hPa. Strong wind speeds and a temperature inversion near mountain-top height, act to trap wave motions within this layer. Given the synoptic shear profile, the presence of Scorer parameter layering, such as that discussed by Durran (1986), and the development of high amplitude wave motions with downslope windstorm-like characteristics are likely.

Overall, AUG24 and NOV13 are characterized by southerly flow near the surface and near-mountain-top wave trapping mechanisms, such as directional shear and Scorer parameter layering. These produce the trapping and reflection of wave motions that amplify the lee waves and produce downslope windstorm-like features near the base of the mountain. The strong synoptic forcing permits the maintenance of cross-mountain wind directions that support the development of these features.

3.3.2 Network Observations

AUG24 is characterized by strong stratification and rapid cooling (~2 K h-1) during the first 3 h of the night (Fig. 3-19a). After 0300 UTC, a 6-K temperature fluctuation is observed at 2 and 9 m AGL. The higher temperature persists through most of the night with the exception of brief cooling episodes taking place between 0500-0530 UTC and 0600-0700 UTC. These brief cooling periods are characterized by strong static stability near the surface. During the first 3 h of the night, the wind speeds are predominantly below 1 m s^{-1}(Fig. 3-19c), and wind directions are highly variable and largely easterly (Fig. 3-19e). However, the sudden warming is accompanied by wind speeds of 3 to 3.5 m s^{-1} and southerly wind directions that fluctuate from southerly to northeasterly as the wind speed fall below 1 m s^{-1} during the brief cooling periods. The southerly

flow indicates downward motion from Tussey Ridge impacting Site 9.

During the first 3 h, this case is also characterized by strong stability, large Ri_b (Fig. 3-19b), low-amplitude, vertical heat flux fluctuations and near 0 m^2 s^2 *TKE* (Fig. 3-19d and f). The
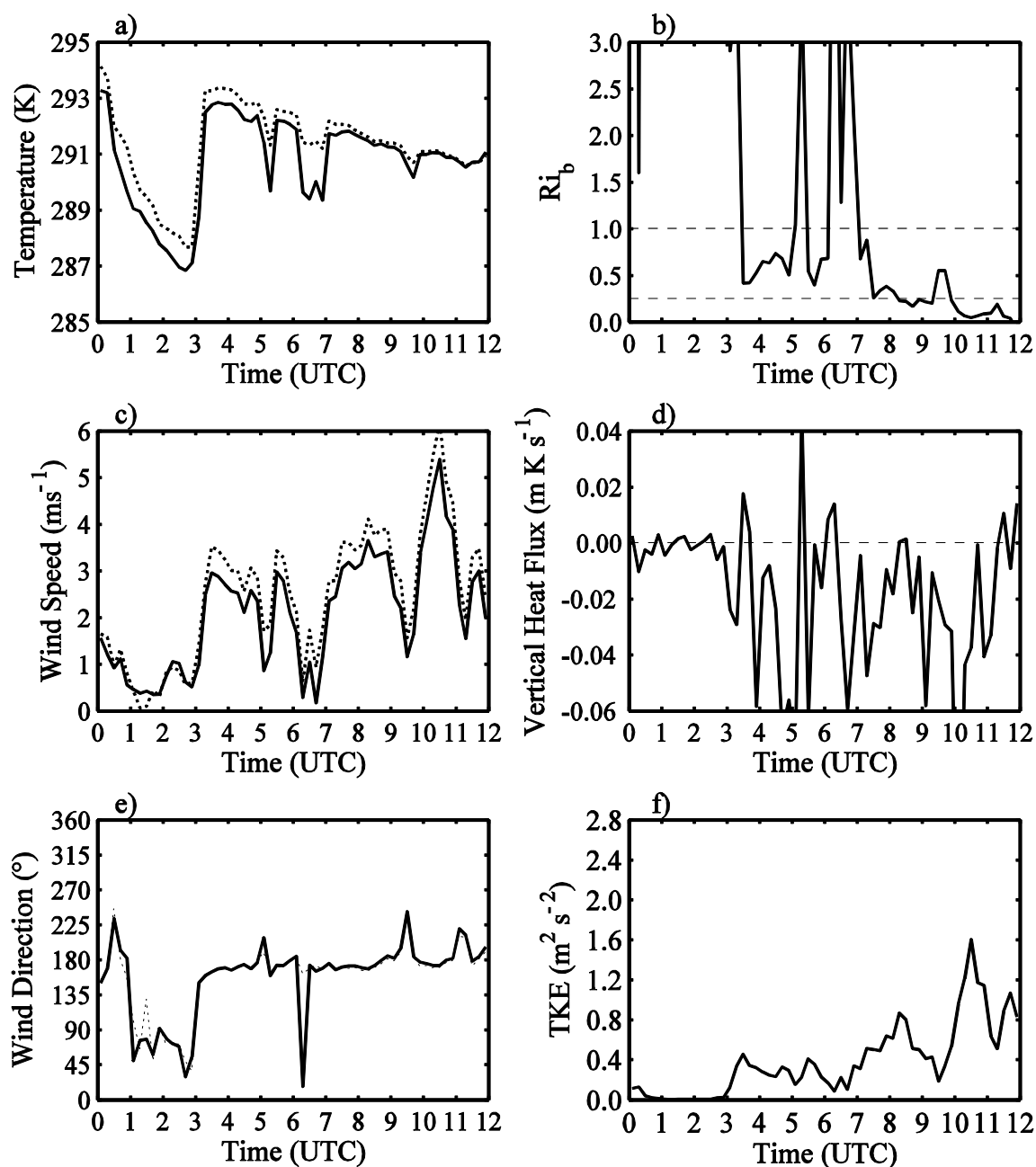
Figure 3-19. Same as Fig. 3-3 but for AUG24.

initial warming period observed after 0300 UTC is associated with a reduction of the Ri_b to

approximately 0.5, positive heat flux and *TKE* increases to approximately 0.4 m2 s2. Turbulent

mixing and positive heat flux (resulting from wave breaking) can decrease the Ri_b. The recurring

warming periods are associated with reduced *Rib*, positive vertical heat flux, and enhanced *TKE*

generation. The brief cooling periods observed from 0500-0530 and 0600-0700 UTC are

associated with high Ri_b and slightly reduced *TKE* values near the surface.

The feature responsible for the large temperature increase observed at 0300 UTC appears

to be horizontally coherent through the network (Fig. 3-20). Sites 3, 9, and 12, located in the

valley and away from the slopes of Tussey Ridge, experience large temperature fluctuations of up

to 7 K during this period. Site 6, located on the slope of Tussey Ridge, experiences little

warming after 0300 UTC and weak fluctuations of up to 1 K through the rest of the night. Site 7,
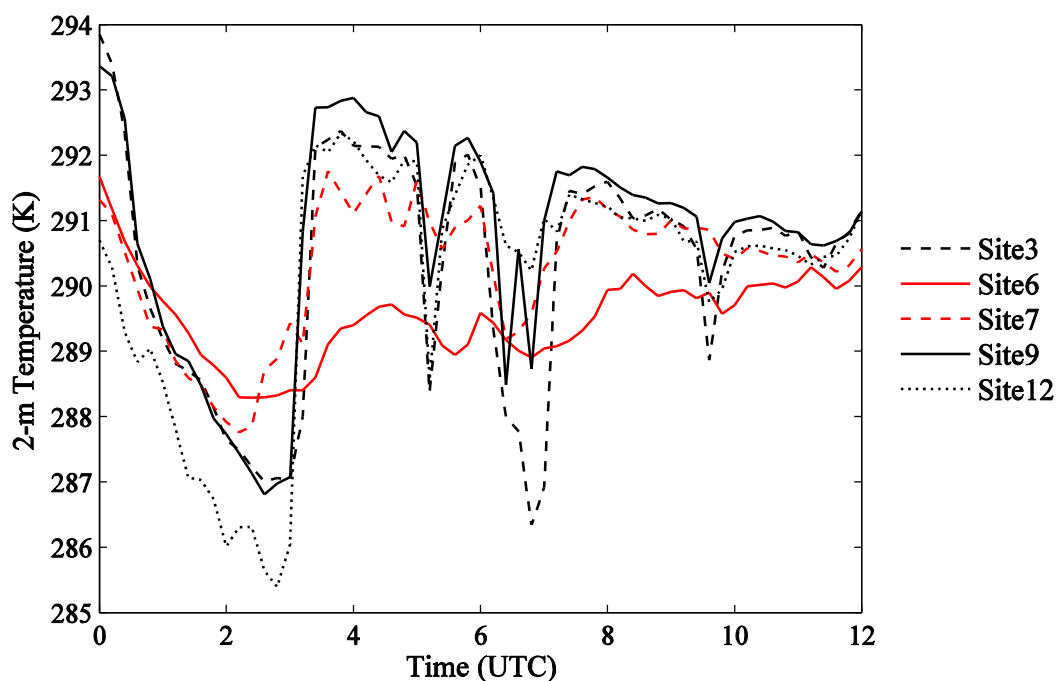
Figure 3-20. Time series of 12-min centered-averaged temperature for multiple sites for AUG24 show temperature fluctuations of up to 7 K throughout the night. Fluctuations are larger for valley sites located deeper within the cold pool. Weakest fluctuations are observed at Site 6, located higher up the slope. Features appear to be horizontally coherent through the network.

located further down the slope, reports fluctuations stronger than Site 6 but weaker than at the other sites after 0300 UTC. Thus, the amplitude of the temperature perturbations are larger for sites located lower within the cold pool (note Site 12) than for sites located higher on the Tussey Ridge slopes.   The source of the temperature fluctuations appears to be propagating away from the ridge since it is observed at Site 7, and then at Sites 3 and 9 consecutively. The opposite behavior is observed during the brief cooling period, where the cooling is observed at site 9, 3, 12, and 7 respectively. This suggests the source mechanism has an oscillatory wavelength. Thus the phenomenon is characterized by rapid changes in wavelength that propagates past the network impacting all sites during the warming periods and rapidly recedes up Tussey's slope during cooling periods, allowing the nearby, cold air back into the network.

SODAR 2027, located in the slope of Tussey Ridge for this case, reveals the presence of generally less than 2 m s^{-1} flow between 0130-0300 UTC (Fig. 3-21a). During this period, southerly cross-mountain flow is present at 30 m AGL. This period is also characterized by very strong directional shear, near-zero vertical motions and little *TKE* generation aloft (Fig. 3-21b). After 0300 UTC, wind speeds exceeding 6 m s^{-1} and extending up to 130 m AGL are observed. The wind directions below 90 m AGL vary from southerly (with a large cross-mountain component), from 0240-0320 UTC, to mostly southwesterly (parallel to the ridge) afterwards. Periods of enhanced *TKE* generation are noted through this period extending from the 30 to 150 m AGL. The SODAR is hypothesized to be in the downward branch of a lee wave. This is supported by the persistently strong downward vertical motions, exceeding 2.0 m s^{-1}, observed within this layer.

It is hypothesized that trapping and reflection of wave motions near mountain top result in the amplification and breaking of a Tussey Ridge lee wave over the observing network. These mechanisms, resembling those of a downslope windstorm, result in stronger wind speeds that act to displace the surface cold pool and produce large temperature fluctuations within the valley.

The trough of the lee wave appears to strongly impact the network and decreases Ri_b, increases

turbulent mixing and results in wave breaking and convective instabilities. During brief periods

throughout the night, the trough of the lee wave may recede up the slope of Tussey and minimize

its impact on the valley surface. This would permit the brief reestablishment of the surface cold

pool.
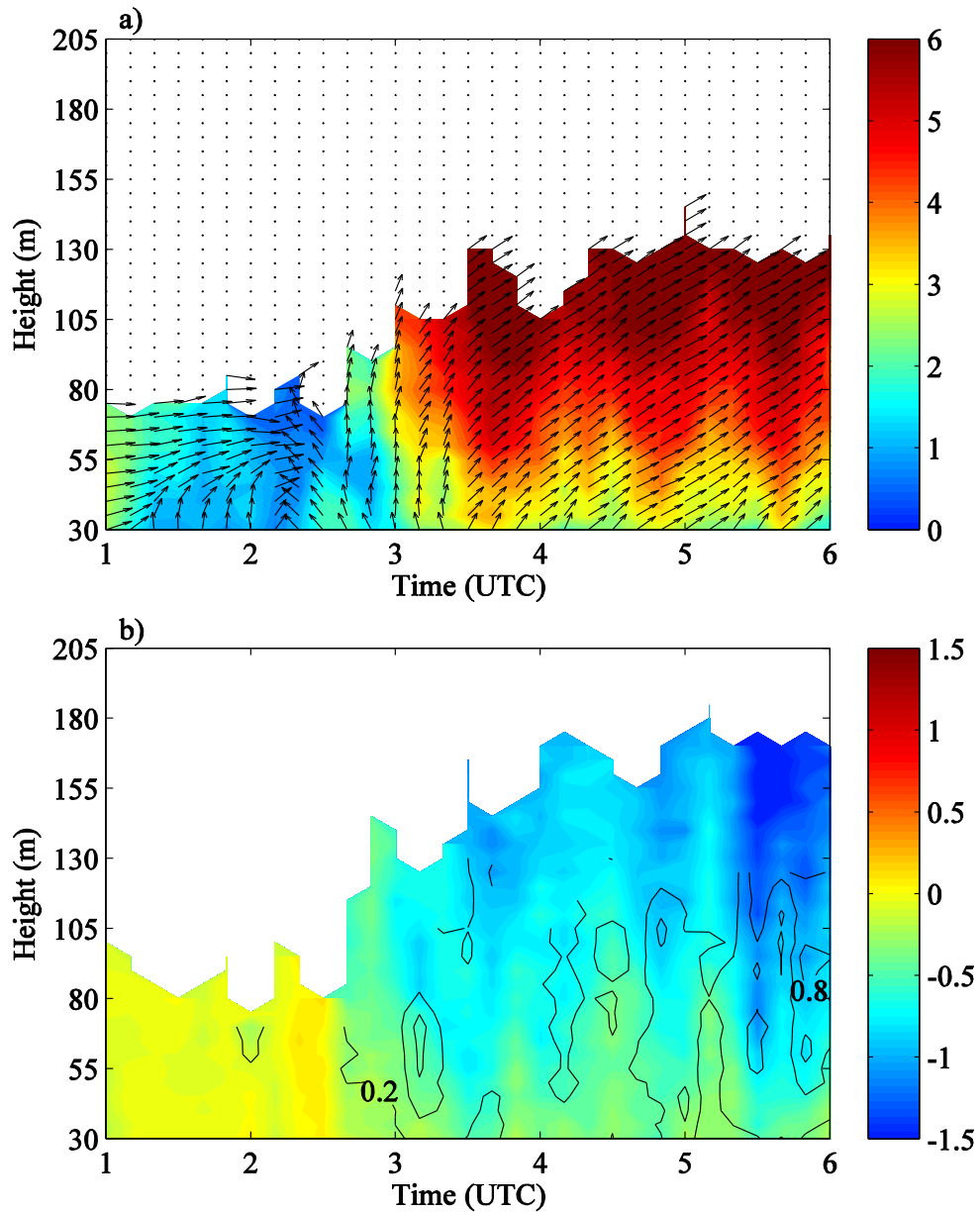
Figure 3-21. As in Fig. 3-5 but for 0100-0600 UTC AUG24

The NOV13 case study is characterized by very strong stratification and light winds through the first 5 h of the night (Fig. 3-22a). The temperature difference between the 2 and 9 m AGL level can be of up to 3.5 K through this period. After 0500 UTC, a rapid increase in temperature of approximately 6 K is observed at Site 9. The temperature change persists for 3 h, and it is followed by rapid cooling that continues until 1000 UTC. At approximately 1030 UTC, another sharp temperature change of ~7 K is observed within the network.

The wind speed and temperature time series present a similar behavior to those in the AUG24 case. Wind speeds generally less than 1 m s^{-1} are observed between 0100-0500 UTC (Fig. 3-22c), and during the period of positive temperature fluctuations, wind speed increases up to 4 m s^{-1}. From 0500-0800 and 1030-1100 UTC, southerly flow dominates throughout the network. Similar to AUG24, the period prior to the onset of the temperature increase is characterized by very large Ri_b (Fig. 3-22b). However, despite Ri_b much greater than 1, positive vertical heat fluxes and TKE up to 0.2 m^2 s^{-2} can be observed at 2 m AGL (Fig. 3-22d and f). Between 0500-0800 UTC, the reduced stability and increased wind speed result in Ri_b values approaching 0.25; and TKE values reach 0.6 m^2 s^{-2} at Site 9. The beginning of this period of increased temperature exhibits positive heat flux, indicating the development of convective instabilities and possible wave breaking.

Temperature fluctuations similar to those observed at Site 9 for NOV13 are also observed at Sites 3 and 12 (Fig. 3-23). Site 12 measures temperature fluctuations of up to 7 K at 0500 UTC while Sites 9 and 3 observe a 5 K temperature increase. Sites 6 and 7, however, do not experience large amplitude temperature fluctuations like those observed within the valley. Finally, Site 8 does not experience the rapid temperature increase observed at other sites after 0500 UTC. However, it measures a temperature drop of 8 K from 0130-0200 UTC, and then experiences a more gradual 9-K temperature increase from 0300-0700 UTC. Overall, sites located lower within the valley experience larger temperature fluctuations than those located up

the slopes of Tussey Ridge. Similarly, valley sites located deeper within the cold pool (sites 8 and 12) can experience temperature changes of up to 9 K due to displacement of the dense, cold air.

During this case study, the SODARs are located within the valley floor. SODAR 2027
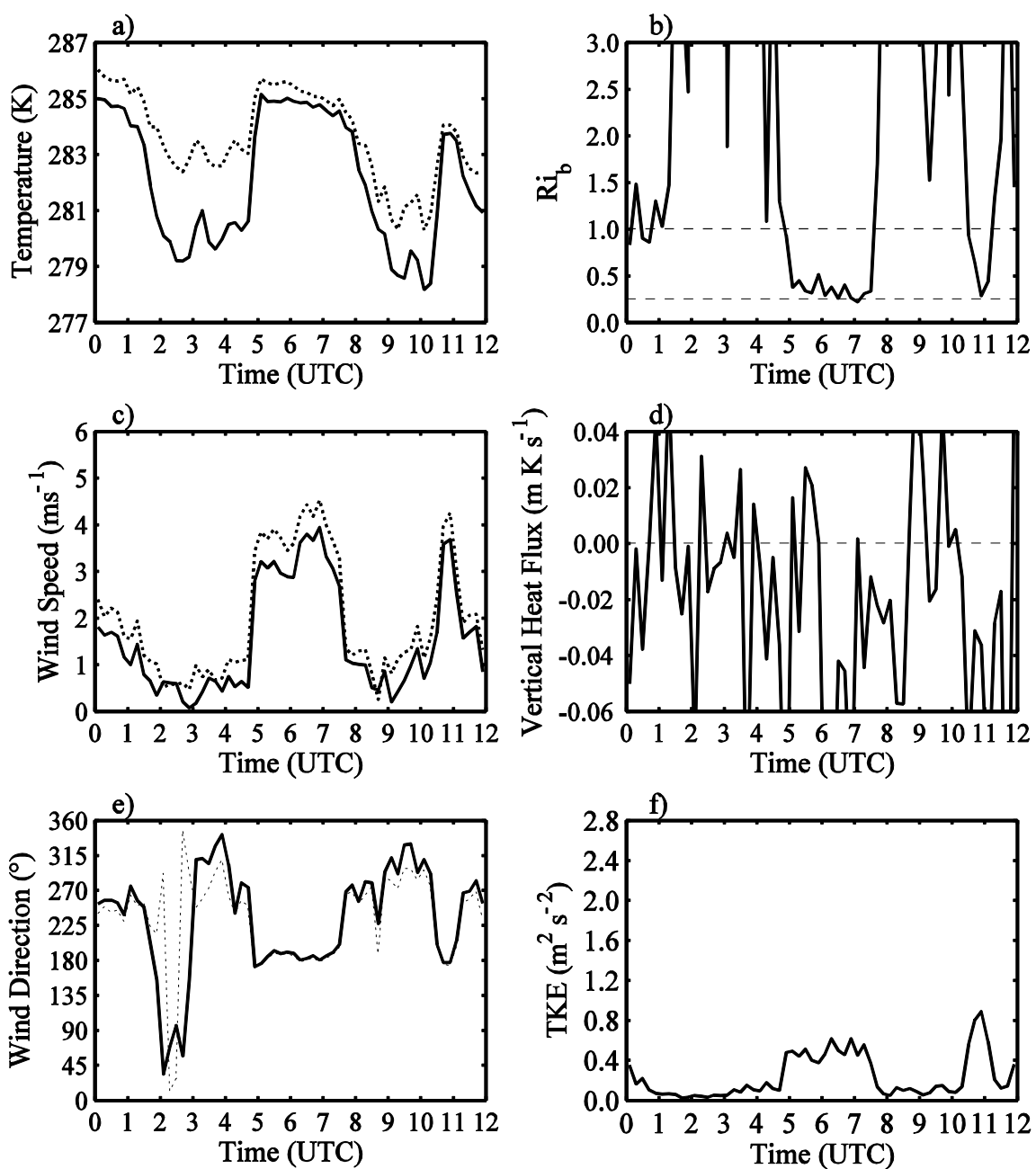
Figure 3-22. As in Fig. 3-3 but for NOV13.

captures the development and evolution of a possible lee wave over the network. This case features weak wind speeds of less than 2 m s^{-1} from 30 to 55 m AGL and wind speeds increasing to more than 6 m s^{-1} above this layer. The presence of flow with a predominantly southwesterly component is observed from 30 to 60 m AGL and higher levels throughout the night. The southerly and southwesterly synoptic flow is observed between 0500-0800 UTC. For this case study, the SODAR is hypothesized to be located in (i.e., beneath) the upward branch of the lee wave crest. This hypothesis is supported by the persistent positive vertical wind velocities measured by the SODAR. Vertical velocities of up to 1.5 m s^{-1} are observed between 0500-0800 UTC extending from 60 to 155 m AGL. The periods of strong downward vertical motions are associated with enhanced *TKE* generation that can extend downward to 35 m AGL
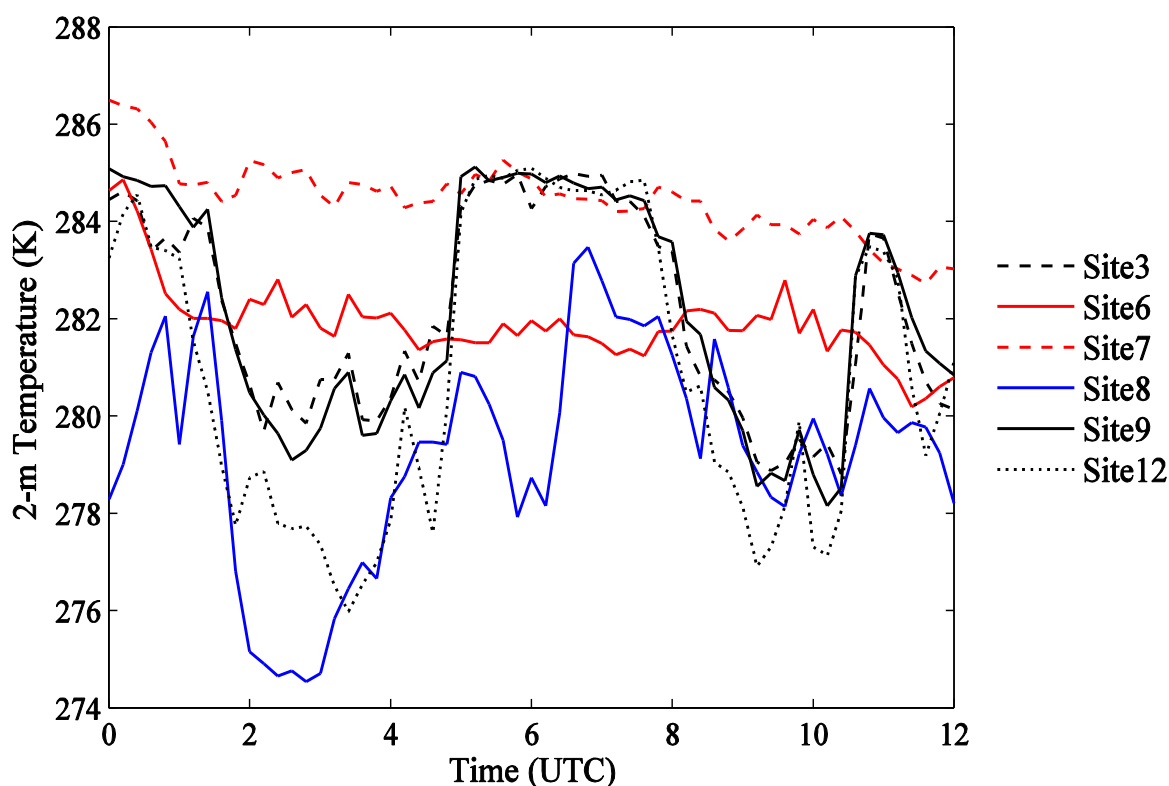
Figure 3-23. Time series of 12-min centered-averaged temperature for multiple sites for NOV13 show temperature fluctuations of up to 7 K throughout the night. Fluctuations are larger for valley sites located deeper within the cold pool. Weakest fluctuations are observed at Site 6 and 7, located higher up the slope. Features appear to be horizontally coherent through the network.
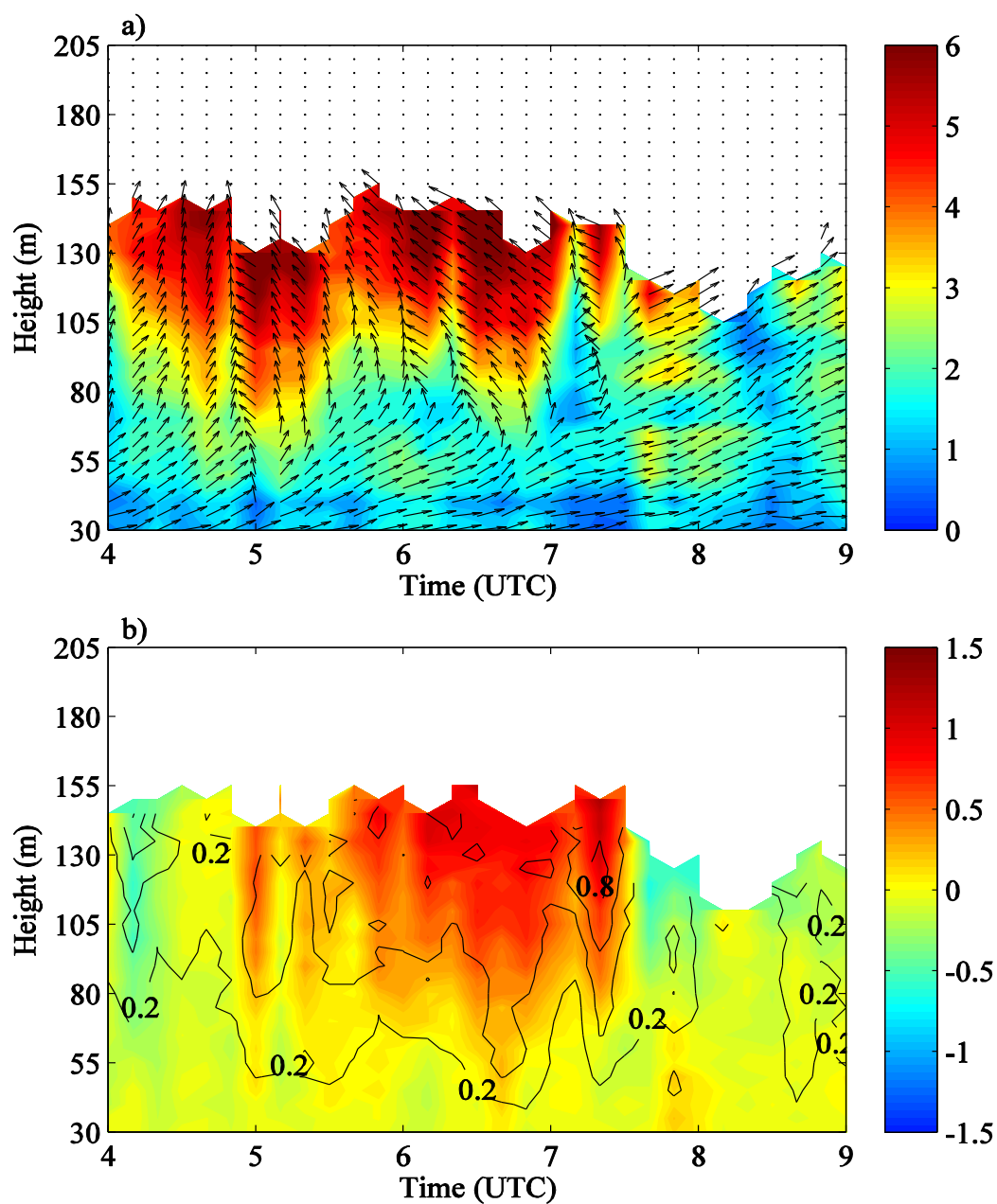
Figure 3-24. As in Fig. 3-5 but for 0400-0900 UTC NOV13.

In this case, a highly nonlinear lee wave is hypothesized to impact the network through the nighttime period.   Through the first 5 h of the night, a deep cold pool develops, characterized by strong static stability and very light winds.   Through wave reflection and/or wave breaking, the lee wave intensifies.   Stronger southerly winds associated with the intensifying lee wave

displace the cold pool near the valley floor, resulting in a sudden warming of up 7 K the lower stations. The stronger winds impact the surface for 3 h. After this period, the lee wave may recede up the slope. The presence of the wind reversal regions aids the advection of the colder air, displaced by the lee wave trough, back towards Tussey Ridge. This may be responsible for the rapid cooling observed between 0800-1000 UTC. The same mechanism is presumed responsible for the increased temperature and wind speed fields observed at 1030 UTC.

Overall, both cases are characterized by rapid low-level temperature and wind changes of up to 7 K and 4 m s^{-1} during periods for which the associated synoptic conditions permit the trapping and amplification of gravity waves through nonlinear processes. As the lee wave intensifies, it can displace the cold pool producing large temperature changes at the surface, reducing the stratification and generating turbulence. This mechanism is hypothesized to be responsible for all the large temperature changes observed in both cases.

CHAPTER 4

SUMMARY AND CONCLUSIONS

The impact of wave-turbulence interactions in the stable boundary layer is investigated using observations and analysis from a special network located at Rock Springs, PA. To the author's knowledge, this is the first time that evidence of wave-induced rotor circulations generated from the moderately complex topography over Eastern US has been provided.

In this study, observational support for the existence of three distinct gravity wave mechanisms that can impact the Rock Springs network is documented. The synoptic background flow has been used to identify the large-scale conditions associated with the development of trapped lee waves within the Nittany Valley. These conditions include strong stability, directional shear, and the development of background critical levels and/or Scorer parameter layering. Three synoptic conditions are identified in which trapped gravity waves may be likely over the Nittany Valley. First, trapped gravity waves excited by the Allegheny Mts. are expected in the presence of stable, westerly or northwesterly flow. Second, trapped lee waves excited by Tussey Ridge are expected in the presence of stable, southerly flow. Finally, downslope windstorm-like wave motions are expected in the presence of southerly or southeasterly flow, weak synoptic forcing, and weak wind shear near mountain top.

Rock Springs network observations are used to identify nonlinear wave interactions and their impact on surface cold pool measurements. Waves induced by the Allegheny Mts. result in temperature and wind speed fluctuations of approximately 1-1.5 K and 0.5-1.5 m s^{-1}. These cases exhibit shallow circulations that resemble Type 1 rotor circulations. The presence of these vortical structures is hypothesized to be responsible for reducing Ri_b, developing convective instabilities, and enhancing shear and buoyant TKE production. Tussey Ridge induced gravity

waves, on the other hand, produce temperature fluctuations of up to 3 K and wind speed fluctuations of approximately 1-5 m s^{-1}. Despite Ri_b ranging from nearly neutral (0) to very stable (>>1), *TKE* values ranging from 0.05-2.6 m^2 s^{-2} can be observed for these cases. Circulations, resembling those of Type 1 rotors, are also observed for these cases. These rotors are presumed responsible for the enhanced *TKE* production and positive vertical heat fluxes observed through the nighttime period. Finally, downslope windstorm-like events excited by Tussey Ridge result in abrupt temperature increases of approximately 5-7 K through the network multiple times throughout the night. These fluctuations are hypothesized to be the result of the displacement of the surface cold pool by an intensifying lee-wave trough. Wind speed fluctuations of up to 4 m s^{-1} reduce the Ri_b and enhance *TKE* shear production. Type 2 rotors are hypothesized as a result of the intense turbulence, strong wind speeds and persistent strong vertical motion observed during these events.

This work is the first part of a combined observation and modeling study designed to investigate the impact of wave-turbulence interactions in the SBL. The observational evidence obtained during this first part of the study provides some clues as to the type of wave induced circulations impacting the SBL over the Rock Springs network. Ongoing and future work related to this research focuses on the investigation of these wave-turbulence interactions and wave breaking, wave-wave interactions and rotors using high resolution numerical models. This includes 1) assessing the efficacy of a high resolution model to resolve these shallow SBL features, 2) examining the model's forecast sensitivity to various initialization strategies and physics, 3) developing and implementing a sophisticated verification strategy that includes the stochastic evaluation of model forecasts for non-deterministic submeso motions, and 4) investigating the impact of rotor circulation and nonstationarity on the surface cold pool.

REFERENCES

Booker, J.R., and F.P. Bretherton, 1967: The critical layer for internal gravity waves in shear flow. *Journal of Fluid Mechanics*, 27, 513-539.

Brown, A.R, M. Athanassiadou, and N. Wood, 2003: Topographically induced waves within the stable boundary layer. *Quart. J. Roy. Meteor. Soc*, 129, 3357-3370.

Blumen, W., R. Banta, S.P. Burns, D.C. Fritts, R. Newson, G.S. Poulos, and J. Sun, 2001: Turbulence statistics of a Kelvin-Helmholtz billow event observed int eh night-time boundary layer during the Cooperative Atmosphere-Surface Exchange Study field program. *Dynamics of the Atmospheres and Oceans*, 34, 189-204.

Clark, T.L, and W.R. Peltier, 1977: On the evolution and stability of finite amplitude mountain waves. *Journal of Atmospheric Sciences*, 34, 1715-1730.

____, and ____, 1984: Critical level reflection and the resonant growth of nonlinear mountain waves. *Journal of the Atmospheric Science*, 41, 3122-3134.

Collis, R.T., F.G. Fernald and J.E. Alder, 1968: Lidar observations of Sierra-wave conditions. *Journal of Applied Meteorology*, 7, 227-233.

DeBaas, A.F., and G.M. Driedonks, 1985: Internal gravity waves in a stably stratified boundary layer. *Boundary-Layer Meteorology*, 31, 303-323.

Dornbrack, A., and C.J. Nappo, 1997: A note on the application of linear wave theory at critical levels. *Boundary-Layer Meteorology*, 82, 399-416.

Doyle, J.D., and D.R. Durran, 2002: The dynamics of mountain-wave-induced rotors. *Journal of the Atmospheric Sciences*, 59, 186-201.

_____, and _____, 2007: Rotor and subrotor dynamics in the lee of three-dimensional terrain. *Journal of Atmospheric Sciences*, 64, 4202-4221.

____, V. Grubisic, W.O.J. brown, S.F.J. de Wekker, A. Dornbrack, Q. Jiang, S.D. Mayor, and M. Weissman, 2009: Observations and numerical simulations of subrotor vortices during T-REX. *Journal of Atmospheric Sciences*, **66**, 1229-1249.

Edwards, N.R., and S. D. Mobbs, 1997a: Observation of isolated wave-turbulence interactions in the stable atmospheric boundary layer. *Quart. J. Roy. Meteorol. Soc.*, **123**, 561-584.
_____, N. R., and _____, 1997b: Modelling isolated wave-turbulence interactions in the stable atmospheric boundary layer. *Quart. J. Roy. Meteorol. Soc.*, **123**, 585-504.

Einaudi, F., and Finnigan, J.J., 1981: The interaction between an internal gravity wave and the planetary boundary layer. Part I: Linear analysis. *Quarterly Journal of the Royal Meteorological Society*, 107, 793-806.

____, and _____, 1993: Wave-turbulence dynamics in the stably stratified Boundary layer. *Journal of the Atmospheric Sciences,* 50, 1841-1864.

Finnigan, J.J., and F. Einaudi, 1981: The interaction between an internal gravity wave and the planetary boundary layer. Part II: Effects of the wave on the turbulence structure. *Quarterly Journal of the Royal Meteorological Society*, 107, 807-832.

_____, J.J., _____, and D. Fua, 1984: The interaction between an internal gravity wave and turbulence in a stably-stratified nocturnal boundary layer. *Journal of Atmospheric Sciences,* 41, 2409-2436.

_____, J, 1999: A note on wave-turbulence interaction and the possibility of scaling the very stable boundary layer. *Boundary-Layer Meteorology*, 90, 529-539.

Fritts, D.C, 1978: The nonlinear gravity wave-critical level interaction. *Journal of Atmospheric Sciences*, 35, 397-413.

Fua, D., G. Chimonas, F. Einaudi, and O. Zeman, 1982: An analysis of wave-turbulence interaction. *Journal of Atmospheric Sciences*, **39**, 2450-2463.

Grubisic, V., and B.J. Billings, 2007: The intense lee-wave rotor event of Sierra Rotors IOP 8. *Journal of Atmospheric Sciences*, 64, 4178-4201.

Gohm, A., G.J. Mayr, A. Fix, and A. Giez, 2008: On the onset of bora and the formation of rotors and jumps near mountain gap, *Quarterly Journal of the Royal Meteorological Society*, **134**, 21-46.

Hertenstein, R.F., and J.P. Kuettner, 2005: Rotor types associated with steep lee topography: Influece of the wind profile. *Tellus*, 57, 117-135.

_____, 2009: Influence of inversions on rotors. *Monthly Weather Review*, 137, 433-446.

Kuettner, J., 1959: The rotor flow in the lee of mountains. Geophysics Research Directorate (GRD) Research Notes 6, AFCRC-TN-58-626, Air Force Cambridge Research Center, USA.

Jeffrey, H., 1925: The flow of water in an inclined channel of rectangular cross section. *Philosophy Magazine*, 49, 793-807.

Lester, P.F. and W.A. Fingerhut, 1974: Lower turbulent zones associated with mountain lee waves. *Journal of Applied Meteorology*, **13,** 54-61.

Mahrt, L., 1999: Stratified atmospheric boundary layers. *Boundary-Layer Meteorology*, 90, 375-396.

____, L., and D. Vickers, 2002: Contrasting vertical structures of nocturnal boundary layers. *Boundary-Layer Meteorology*, 105, 351-363.

____, L, 2007: Weak-wind mesoscale meandering in the nocturnal boundary layer. *Environmental Fluid Mechanics*, 7, 331-347.

____, L., and R. Mills, 2009: Horizontal diffusion by submeso motions in the stbale boundary layer. *Environmental Fluid Mechanics*, 9, 443-456.

____, L., S. Richardson, N. Seaman, D. R. Stauffer, 2010: Non-stationary drainage flows and motions in the cold pool. *Tellus*, 62A, 698-705.

____, L., C. Thomas, S. Richardson, N. Seaman, D. Stauffer, and M. Zeeman, 2012a: Nonstationary generation of weak turbulence for very stable and weak-wind conditions. *Boundary Layer Meteorology*, DOI 10.1007/s10546-012-9782-x.

____, S. Richardson, N. Seaman, D. Stauffer, 2012b: Turbulence in the nocturnal boundary layer with light and variable winds. *Q. J. R. Meteorol. Soc.*, DOI:10.1002/qj.1884

Mestayer, P.G., and S. Anquetin, 1995: Climatology of cities. *Diffusion and Transport of Pollutants in Atmospheric Mesoscale Flow Fields,* A. Gyr and F.-S. Rys, Eds., Klumer Academics, 165-189.

Mobbs, S. D., S. B. Vosper, P. F. Sheridan, R. Cardoso, R. R. Burton, R. R. Arnold, M. K. Hill, V. Horlacher, and A. M. Gadian, 2005: Observations of downslope winds and rotors in the Falkland Islands. *Q.J.R. Meteorol. Soc.*, **131**, 329–351.

Nance, L.B, and D.B. Durran, 1997: A modeling study of nonstationary trapped mountain lee waves. Part I: Mean-Flow Variability. *Journal of Atmospheric Sciences,* 54, 2275-2291.

____, and ____, 1998: A modeling study of nonstationary trapped mountain lee waves. Part II: Nonlinearity. . *Journal of Atmospheric Sciences,* 55, 1429-1445.

Nappo, C., 1991: Sporadic breakdowns of stability in the PBL over simple and complex terrain. *Boundary-Layer Meteorology*, 54, 69-87.

_____, C., and G. Chimonas, 1992: Wave exchange between the ground surface and a boundary-layer critical level. *Journal of Atmospheric Sciences*, 49, 1075-1091.

_____, C., 2002: An introduction to atmospheric gravity waves. *Academic Press*, New York.

_____, H-Y. Chun, and H-J. Lee, 2004: A parameterization of wave stress in the planetary boundary layer for use in mesoscale models. *Atmospheric Environment*, 38, 2665-2675.

Newson, R.K., and R.M. Banta, 2003: Shear-flow instability in the stable nocturnal boundary layer as observed by Doppler lidar during CASES-99. *Journal of the Atmospheric Sciences*, 60, 16-33.

Ralph, F.M., P.J. Neiman, T.L. Keller, D. Levinson, and L. Fedor, 1997: Observation, simulations and analysis of nonstationary trapped lee waves. *Journal of Atmospheric Sciences,* 54, 1308-1333.

Reynolds, W.C., and A.K.M.F. Hussain, 1972: The mechanics of an organized wave in turbulent shear flow. Part 3. Theoretical models and comparisons with experiments. *Journal of Fluid Mechanism*, 54, 263-288.

Salmond, J.A., and I.G. McKendry, 2005: A review of turbulence in the very stable nocturnal boundary layer and its implications for air quality. *Progress in Physical Geography,* 29, 171-188.

Seaman, N.L., B.J. Gaudet, D. R. Stauffer, L. Mahrt, S.J. Richardson, J.R. Zielonka, and J.C. Wyngaard, 2012: Numerical prediction of the submesoscale flow in the nocturnal boundary layer over complex terrain. *Mon. Wea. Review*, 140, 956-997.

Sheridan, P.F. and S.B. Vosper 2006: A flow regime diagram for forecasting lee waves, rotors and downslope winds. *Meteor. Appl.* **13**, 179-195.

Smith, R.B., 1979: The influence of mountains in the atmosphere. *Advance Geophysics*, **21**, 87-230.

_____, 1989: Hydrostatic airflow over mountains. *Advance Geophysics*, **31**, 1-41.

Smith, G.M., and E.D. Skyllingstad, 2009: Investigation of upstream boundary layer influence on mountain wave breaking and lee way rotors using a large eddy simulation. *Journal of the Atmospheric Sciences*, **66**, 3147-3164.

Steeneveld, G.J., 2011: Stable boundary layer issues. *ECMWF GABLS Workshop on Diurnal cycles and the stable boundary layer*, 7-10 November 2011.

Sun, J., S.P. Burns, D.H. Lenschow, R. Banta, R. Newson, R. Coulter, S. Frasier, T. Ince, C. Nappo, J. Cuxart, W. Blumen, X. Lee, and X. Hu, 2002: Intermittent turbulence associated with density current passage in the stable boundary layer. *Boundary-Layer Meteorology*, 105, 199-219.

__, J., D.H. Lenschow, S.P. Burns, R. Banta, R. Newson, R. Coulter, S. Frasier, T. Ince, C. Nappo, B. Balsley, M. Jensen, L. Mahrt, D. Miller, and B. Skelly, 2004: Atmospheric disturbances that generate intermittent turbulence in the nocturnal boundary layer. *Boundary-Layer Meteorology*, 110, 255-279.

___, J., L. Mahrt, R.M. Banta, Y.L. Pichigina, 2012: Turbulence regimes and turbulence intermittency in the stable boundary layer. *Journal of Atmospheric Sciences*, 69, 338-351.

Tjernstrom, M., B.B. Balsley, G. Svensson, and C.J. Nappo, 2009: The effect of critical layers on residual layer turbulence. *Journal of the Atmospheric Sciences*, 66, 468-480.

Udina, M., M.R. Soler, S. Viana, and C. Yague, 2012: Model simulation of gravity waves triggered by a density current. *Quarterly Journal of the Royal Meteorological Society*, DOI:10.1002/qj.2004.

Vergeiner, I., and D.K. Lilly, 1970: the dynamic structure of lee wave flow as obtained from ballon and airplane observations. *Monthly Weather Review*, 98, 1315-1326.

Viana, S., C. Yague, and G. Maqueda, 2009: Propagation and effects of a mesoscale gravity wave over a weakly-stratified nocturnal boundary layer during the SABLES2006 field campaign. *Boundary-Layer Meteorology,* 133, 165-188.

Vickers, D., and L. Mahrt, 2004: Evaluating formulations of stable boundary layer height. *Journal of Applied Meteorology*, 43, 1736-1749.

Vosper, S.B., 2004: Inversion effects on mountain lee waves. *Quaterly Journal of the Royal Meteorological Society*, **130,** 1723-1748.

Weiss, C.E., 1976: Diurnal variation in the wavelength of lee standing waves. NOAA/National Weather Service/National Environmental Satellite Service, Satellite Applications Information Note 76/14, NOAA-S/T 76-2404, National Environmental Satellite Service, Washington, DC, 7

Zaveri, R.A, R.D. Saylor, L.K. Peters, R. McNider, and A. Song, 1995: A model investigation of the summertime diurnal ozone behavior in rural mountainous locations. *Atmospheric Environment*, 9, 1043-1065.